IMPLEMENTATION OF DIGITAL DETECTION SCHEME FOR FIBER OPTIC GYROSCOPE

A THESIS

SUBMITTED TO THE DEPARTMENT OF ELECTRICAL AND

ELECTRONICS ENGINEERING

AND THE GRADUATE SCHOOL OF ENGINEERING AND SCIENCE

OF BILKENT UNIVERSITY

IN PARTIAL FULFILLMENT OF THE REQUIREMENTS

FOR THE DEGREE OF

MASTER OF SCIENCE

By

Serdar Öğüt

August, 2013

I certify that I have read this thesis and that in my opinion it is fully adequate, in scope and in quality, as a thesis for the degree of Master of Science.

Prof. Dr. Orhan Aytür (Advisor)

I certify that I have read this thesis and that in my opinion it is fully adequate, in scope and in quality, as a thesis for the degree of Master of Science.

Prof. Dr. Ekmel Özbay

I certify that I have read this thesis and that in my opinion it is fully adequate, in scope and in quality, as a thesis for the degree of Master of Science.

Assist. Prof. Dr. F. Ömer İlday

Approved for the Graduate School of Engineering and Science:

Prof. Dr. Levent Onural
Director of the Graduate School

ABSTRACT

IMPLEMENTATION OF DIGITAL DETECTION SCHEME FOR FIBER OPTIC GYROSCOPE

Serdar Öğüt
M.S. in Electrical and Electronics Engineering
Supervisor: Prof. Dr. Orhan Aytür
August, 2013

Fiber optic gyroscope (FOG) is a kind of inertial sensor that can be used for navigation, control and guidance of air, naval, land and space vehicles. A FOG measures rotation rate dependent on phase difference between two counter-propagating light waves through a rotating fiber loop. In this thesis, the main principles of FOG such as Sagnac effect and reciprocity are described. The optical scheme consists of a broadband light source, a coupler, a polarizer, an integrated optic chip and a fiber coil, is developed and established.

The modulation and demodulation techniques used in FOG are also investigated in detail. The digital detection system is built with a photodetector, a transimpedance amplifier, a voltage amplifier and a data acquisition (DAQ) system. A transceiver module and an FPGA processor are the components of DAQ system. The modulation and demodulation processes are implemented by using LabVIEW FPGA module. The program created in LabVIEW environment allows to characterize scale factor and phase modulator parameters. Rotation rate measurements are performed and analyzed by Allan variance method.

The impacts of different noise types to the performance of FOG are analyzed. Angle random walk (ARW), noise component to determine short-term accuracy of FOG, is reduced by integration of spike-free signal. We also show that we obtain similar noise parameters even if the output power of the system is very low. It is proven and tested that ARW is reduced by the optimization of modulation depth. Theoretical and experimental results are quite consistent at every stages of the work.

Keywords: fiber optic gyroscope, FOG, Sagnac effect, square-wave bias modulation, angle random walk.

ÖZET

FİBER OPTİK DÖNÜÖLÇER İÇİN SAYISAL ALGILAMA ŞEMASININ GERÇEKLENMESİ

Serdar Öğüt
Elektrik ve Elektronik Mühendisliği, Yüksek Lisans
Tez Yöneticisi: Prof. Dr. Orhan Aytür
Ağustos, 2013

Fiber optik dönüölçer (FOD), bir çeşit ataletsel sensör olup hava, deniz, kara ve uzay araçlarının seyrüsefer, kontrol ve yönlendirmeleri için kullanılabilmektedir. FOD, dönen bir fiber döngüsü boyunca aksi yönlerde yayılan iki ışık dalgası arasında faz farkına bağlı dönü hızını ölçer. Bu tez çalışmasında, FOD'un Sagnac etkisi ve karşılıklılık gibi temel prensipleri anlatılmıştır. Geniş bantlı bir ışık kaynağı, çiftleyici, kutuplayıcı, bütünleşik optik yonga ve fiber sarımdan oluşan optik şema geliştirilmiş ve kurulmuştur.

FOD'da kullanılan modülasyon ve demodülasyon teknikleri ayrıntılı olarak incelenmiştir. Fotodetektör, transempedans yükseltici, gerilim yükseltici ve veri toplama sistemi ile sayısal algılama sistemi kurulmuştur. Alıcı-verici modül ve FPGA işlemci, veri toplama sisteminin bileşenleridir. Modülasyon ve demodülasyon süreçleri LabVIEW FPGA modülü kullanılarak gerçeklenmiştir. LabVIEW ortamında oluşturulmuş program, orantı katsayısı ve faz modülatörü parametrelerini karakterize etmeye olanak sağlamaktadır. Dönü hızı ölçümleri yapılmış ve Allan varyans yöntemi ile analiz edilmiştir.

Farklı gürültü tiplerinin FOD performansına etkileri incelenmiştir. FOD'un kısa-vadeli doğruluğunu belirleyen gürültü bileşeni açı rasgele yürüme, sivri uçtan bağımsız sinyalin sayısal entegrasyonu ile düşürülmüştür. Aynı zamanda, sistemin çıkış gücü çok düşük olsa bile benzer gürültü parametrelerini elde ettiğimiz gösterilmiştir. Modülasyon derinliğinin optimizasyonu ile açı rasgele yürüme değerinin düşürüldüğü kanıtlanmış ve test edilmiştir. Teorik ve deneysel sonuçlar işin her aşamasında oldukça tutarlıdır.

Anahtar sözcükler: fiber optik dönüölçer, FOD, Sagnac etkisi, kare-dalga kutuplanma modülasyonu, açı rasgele yürüme.

Acknowledgement

First and foremost, it gives me great pleasure to express my gratitude to my advisor, Prof. Dr. Orhan Aytür, for the continuous support, patient guidance, immense knowledge and useful critiques of this research work. I could not have imagined having a better advisor and mentor for my M.S. study.

I would also like to express my sincere gratitude to Prof. Dr. Ekmel Özbay, for his advice, enthusiastic encouragement and enduring patience. He always provided clear explanations when I was lost, and always giving me his time, in spite of anything else that was going on. Besides, I would like to extend my sincerest thanks and appreciation to Assist. Prof. F. Ömer İlday for his invaluable help and insightful comments.

I would like to thank my colleagues in Nanotam, especially Dr. Mutlu Gökkavas, Önder Akçaalan, Aylin Karagöz, Seval Dönertaş, Yasemin Aşık, Evren Öztekin and Ünal Çiftçier for their cooperation, help and friendship. Special thanks go to Berk Osunluk and Alper Bayrı for their valuable ideas and contributions.

I am so grateful to my dearest friends Uğur Yıldız, Sinan Yıldırım, Enes Yılmazer, Okan İnaltay, Merve Yüksel, Çağrı Uzunoğlu, Çağrı Uysal, Gülesin Eren, Emrecan Demirörs, Göktuğ Çınar, Arcan Ertürk, Oya Erkan, Kemal Şen and Orkun Özen for their moral support.

I also appreciate the financial support from the Scientific and Technical Research Council of Turkey (TUBITAK).

Last, but certainly not least, I owe my loving thanks and heartfelt appreciation to my mother, my brother Şevki, my grandma and grandpa for their undying love, continuous support and encouragement.

Contents

1 Introduction **1**

2 Construction of a Fiber Optic Gyroscope **5**

2.1 Basics of Fiber Optic Gyroscope 5

2.1.1 Sagnac Effect 5

2.1.2 Reciprocity 8

2.2 Optical Configuration of Fiber Optic Gyroscope 9

2.2.1 Fiber Coil 11

2.2.2 Light Source 12

2.2.3 Coupler 14

2.2.4 Polarizer 15

2.2.5 Multifunctional Integrated Optical Chip 16

3 Modulation and Demodulation Techniques in Fiber Optic Gyroscope **17**

3.1 Interference Signal 17

3.2 Square-wave Bias Modulation Technique in FOG 18

3.3 Demodulation Techniques in FOG 22

3.4 Closed Loop Fiber Optic Gyroscope 25

3.5 Analog Approach for Preprocess Before Demodulation 28

4 Digital Detection System of Fiber Optic Gyroscope 30

4.1 Configuration of Digital Detection System 30

4.1.1 Photodetector 32

4.1.2 Transimpedance Amplifier 32

4.1.3 A/D and D/A Conversion 34

4.2 Implementation of the Software 36

4.3 Fundamental Experiments 36

4.3.1 Scale Factor Measurements 36

4.3.2 Characterization of the Phase Modulators 37

4.3.3 Rotation Rate Measurements and Allan Variance Method . 38

5 Optimization of Digital Detection Scheme of Fiber Optic Gyroscope 43

5.1 Noise Analysis of Fiber Optic Gyroscope 43

5.1.1 Shot Noise 45

5.1.2 Relative Intensity Noise 47

5.1.3 Electronic Noise 49

5.1.4 Total Noise 55

5.2 Noise Reduction Methods in Fiber Optic Gyroscope 56

5.2.1 Digital Integration of Signal in a Semi-period 56

5.2.2 Required Power Analysis 58

5.2.3 Optimization of Modulation Depth 59

6 Conclusion **62**

List of Figures

2.1 Sagnac effect in a rotating fiber loop [19]. 6

2.2 Reciprocal configuration of a FOG [19]. 8

2.3 Optical configuration of the FOG. 10

2.4 The measurement of the fiber coil's length with OTDR. 12

2.5 Configuration of the ASE light source. 13

2.6 Optical spectrum of the light source. 15

2.7 The structure of MIOC [10]. 16

3.1 Interference signal [19]. 18

3.2 The configuration of a FOG with photodetection, modulation and rotation rate signals [10]. 19

3.3 Photodetector signals with and without rotation when square-wave bias modulation is applied [19]. 21

3.4 The output (*blue*) and modulation (*green*) signals in the cases of absence and presence of rotation. 21

3.5 Feedback algorithm in closed loop FOG [10]. 25

3.6 Digital phase ramp signal in closed loop FOG [15]. 26

3.7 Digital phase ramp, photodetector and square-wave modulation signals in open and closed loop FOGs [19]. 27

3.8 Resetting process in closed loop scheme [10]. 28

3.9 Spike-free signal obtained after analog switch circuit. 29

3.10 Integrated signal in every τ period. 29

4.1 Configuration of the digital detection system. 31

4.2 PXI system included a chassis, a controller and an FPGA module with a transceiver adapter module. 32

4.3 Block diagram of the transceiver adapter module [27]. 34

4.4 The user-interface implemented in LabVIEW environment. 36

4.5 Single-axis rate and position table in NANOTAM. 37

4.6 Intensity vs. phase shift. 38

4.7 Drift and noise in rotation rate data [10]. 39

4.8 Noise types for fiber optic gyroscopes defined in IEEE Standards [30]. 40

4.9 Earth's rotation rate measurement for 12 hrs. 41

4.10 Allan variance curve. 41

5.1 Shot noise vs. modulation depth. Noise to signal ratio is normalized to the corresponding value at $\pi/2$ modulation depth. 47

5.2 Relative intensity noise vs. modulation depth. Noise to signal ratio is normalized to the corresponding value at $\pi/2$ modulation depth. 49

5.3 Equivalent circuit of a TIA driven by a photodiode including noise sources [35]. 50

5.4 Electronic noise vs. modulation depth. Noise to signal ratio is normalized to the corresponding value at $\pi/2$ modulation depth. . 53

5.5 ARW vs. the ratio of number of integrated samples to total samples. 57

5.6 Contribution of different noise types to ARW as a function of power. 58

5.7 ARW vs. power at different TIA gains. 59

5.8 ARW vs. modulation depth for different intensities. 60

5.9 Allan variance curves obtained for standard and optimized modulation techniques. 61

List of Tables

5.1 Noise parameters of TIA 51

5.2 Optimum parameters 61

Chapter 1

Introduction

Fiber optic gyroscope (FOG) is an inertial sensor used for navigation, control and guidance of moving platforms such as air, naval, land and space vehicles. FOGs, essentially all gyroscopes, measure the angular rate around fixed axes with respect to an inertial space. The most common application of FOGs is within inertial navigation systems (INS). An INS is directly mounted on the vehicle and allows its position and velocity estimation without the support of any signal generated by positioning systems such as Global Positioning System (GPS) [1].

Furthermore, the performance of FOGs can be optimized for some other specific applications such as missile and torpedoes guidance, flight controls, gyro compassing, target acquisition systems, electro-optic/forward looking infrared (EO/FLIR) systems and radar stabilization, earth observation satellites, telecom and scientific satellites in addition to inertial navigation systems [2].

The working principle of FOG is based on Sagnac effect. Sagnac demonstrated Sagnac interferometer in 1913 by injecting light from an optical source through a beam splitter such that it moves in two directions around a loop [3, 4]. However, Sagnac's structure was far from measuring rotation rate. In 1925, Michelson and Gale could measure the earth's rotation by using an interferometer with a perimeter of almost 2 km to increase sensitivity [5].

The idea of using a laser interferometer to read the Sagnac phase shift in a closed-cavity path was an attractive idea since the very early time of the laser history. He-Ne laser was discovered in 1961 and it was ideally suited for interferometry. In 1962, Rosenthal proposed to enhance the sensitivity with a ring laser cavity [6]. Just a year later, in 1963, the detection of earth's rotation in a 1 m side square-cavity built around He-Ne tubes was reported by Macek and Davis [7, 8].

In the 1970s, it became possible to use a multiturn optical fiber coil instead of a ring laser with the effort on development of low-loss optical fiber, solid-state semiconductor light source and detector for telecommunication industry. After proposing of fiber optic gyroscope by Pircher and Hepner in 1967 and a coil of optical fiber by Brown in 1968, Vali and Shorthill demonstrated it experimentally in 1976. It was a new approach using the newly developed single-mode fibers as the propagation medium [8–10].

During the past 37 years, several universities and companies such as McDonnell Douglas, Northrop-Grumman (Litton) and Honeywell have investigated the FOG. It has been in production by several companies for more than 20 years.

There are variants of gyroscopes having different working principles. The classical mechanical gyro relies on a spinning mass. They tend to be heavy and complex with a high number of moving parts. Working principle of ring laser gyroscope (RLG) is also based on Sagnac effect. In a RLG, the light from the laser travels through a mixture of inert He-Ne gas within a pressurized cavity of specially polished glass. While RLGs can work in high accuracy, they need dithering to break out of locked-in state. Lastly, in recent years, designers took a new approach by devising a class of miniaturized heading and orientation sensors called micro-electromechanical systems (MEMS). While MEMS are small and relatively inexpensive, they remain too inaccurate for precision applications because of high bias over temperature as well as large noise errors [11].

Consequently, comparing to other gyroscopes, FOGs have severel advantages. Some unique advantages that FOG offers over the other types of gyroscopes are listed in [12] as:

- True solid-state device containing no moving parts,
- No dithering is required,
- Sensitivity can be increased by adding more fiber wraps,
- Tends itself to miniaturization,
- High reliability,
- Long lifetime,
- Rapid turn-on time.

FOGs are categorized by the techniques employed to sense the rotation-induced Sagnac phase shifts. While an interferometric fiber optic gyroscope (IFOG) uses fringe pattern examination, a resonator fiber optic gyroscope (RFOG) employs resonant fiber cavities to sense the Sagnac effects. RFOG has received less attention to date and it is less mature technology. IFOG is presently far more highly developed, with several companies actively engaged in the commercialization of systems developed in recent years [13]. In this thesis, we focus on IFOG.

In the literature, there are several works regarding the detection schemes and signal processing techniques for FOG. However, as Ruffin mentioned, the design details are not published in open literature due to proprietary restrictions although the theoretical basis for FOG operation is published worldwide [12]. In this thesis, we also design and establish the digital detection system for FOG. However, we concentrate on optimization of detection scheme. Investigation of different noise sources is also a part of this thesis.

The theories of modulation and demodulation techniques are given in [10, 14–16]. These works focus on conventional square-wave bias modulation technique while we attempt to optimize modulation depth in order to reduce noise. The effect of modulation depth on different noise types were discussed in [17] and [18]. Furthermore, there is no significant work investigating required output optical

power for optimal performance, in the literature. However, we aim to answer the question of how the output optical power influences the performance of FOG.

One of the most powerful aspects of this thesis is that the theoretical results are supported with experimental results. A FOG is established with both optical and electronic components. The detection system consists of a photodetector, a transimpedance amplifier and a data acquisition (DAQ) system including an FPGA processor and a transceiver. The digital detection scheme is implemented by using LabVIEW FPGA module which offers a powerful graphical programming for FPGA hardware.

The rest of this thesis is organized as follows: Chapter 2 presents the main principles of FOG and introduces the concepts of Sagnac effect and reciprocity. The optical configuration of the FOG is also described. Chapter 3 gives the modulation and demodulation techniques in FOG. Square-wave bias modulation technique is presented in detail. In Chapter 4, implementation of digital detection scheme are explained. Some basic measurements are presented. Chapter 5 focuses the optimization of FOG. The effects of different noise sources on performance and ARW reduction methods are investigated. Finally, Chapter 6 concludes the thesis with a review of our work and a summary of open research topics.

Chapter 2

Construction of a Fiber Optic Gyroscope

2.1 Basics of Fiber Optic Gyroscope

2.1.1 Sagnac Effect

The principle of operation of the FOG is based on Sagnac effect which produces a phase difference in a ring interferometer [10]. Figure 2.1 illustrates the Sagnac effect considering an ideal circular path. A phase shift occurs between two counter-propagating waves in a circular path (in this case, fiber loop with N turns) due to rotation. A FOG measures rotation rate depending on the phase shift. The derivation of Sagnac effect in the circular path is given as follows.

Time for light waves travelling through clockwise (CW) and counter-clockwise (CCW) directions to complete N turns:

$$t_{cw} = \frac{R(2\pi N + \Omega t_{cw})}{c} \tag{2.1a}$$

$$t_{ccw} = \frac{R(2\pi N - \Omega t_{ccw})}{c} \tag{2.1b}$$

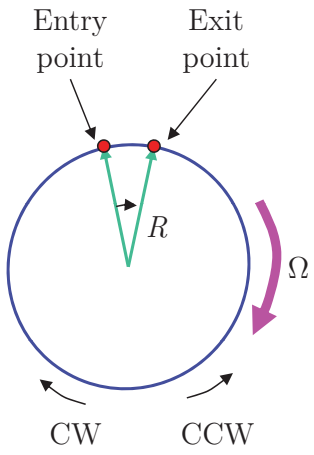

Figure 2.1: Sagnac effect in a rotating fiber loop [19].

where Ω is the angular velocity, R is the fiber loop radius and c is the speed of light.

t_{cw} and t_{ccw} can be found as:

$$t_{cw} = \frac{2\pi RN}{c - R\Omega} \tag{2.2a}$$

$$t_{ccw} = \frac{2\pi RN}{c + R\Omega} \tag{2.2b}$$

Time difference between t_{cw} and t_{ccw} is:

$$\Delta t = t_{cw} - t_{ccw} = \frac{4\pi R^2 N\Omega}{c^2 - R^2\Omega^2} \tag{2.3}$$

Since $c^2 \gg R^2\Omega^2$, we obtained:

$$\Delta t \approx \frac{4\pi R^2 N\Omega}{c^2} \tag{2.4}$$

Substituting loop diameter, $D = 2R$ and loop length, $L = 2\pi RN$:

$$\Delta t \approx \frac{LD\Omega}{c^2} \tag{2.5}$$

Phase shift is found as follows where λ is the working wavelength:

$$\Delta\phi = \omega\Delta t = \frac{2\pi c\Delta t}{\lambda} \tag{2.6}$$

Finally, substituting Equation (2.5) into Equation (2.6), Sagnac effect can be obtained as:

$$\Delta\phi = \frac{2\pi LD}{\lambda c}\Omega \tag{2.7}$$

Fiber loop element in a FOG is called as fiber coil. Apparently, Sagnac effect depends on angular velocity (Ω), working wavelength (λ) and fiber coil parameters which are total fiber length (L) and mean diameter (D).

The proportionality constant between phase shift and angular velocity is defined as scale factor. It is generally used to define the precision of FOG and its unit is s. Scale factor formula is given in Equation (2.8).

$$SF = \frac{2\pi LD}{\lambda c} \tag{2.8}$$

While the working wavelength is 1550 nm, for a fiber coil with a mean diameter of 3 cm and a length of 200 m, scale factor is found as follows:

$$SF = \frac{2\pi \cdot 200\ m \cdot 3\ cm}{1550\ nm \cdot 3 \cdot 10^8\ m/s} = 0.081\ s \tag{2.9}$$

The angular speed of earth's rotation can be expressed as 15.041 $^\circ/hr$. A gyroscope standing on a flat table in Ankara measures the earth's rotation rate proportional to the sine function of the longitude. Since the longitude of Ankara is $39^\circ 56' = 39.93^\circ$, the earth's rotation rate in Ankara can be found as:

$$\Omega = 15.041^\circ/hr \cdot \sin(39.93^\circ) = 9.65^\circ/hr = 4.68 \cdot 10^{-5}\ rad/s \tag{2.10}$$

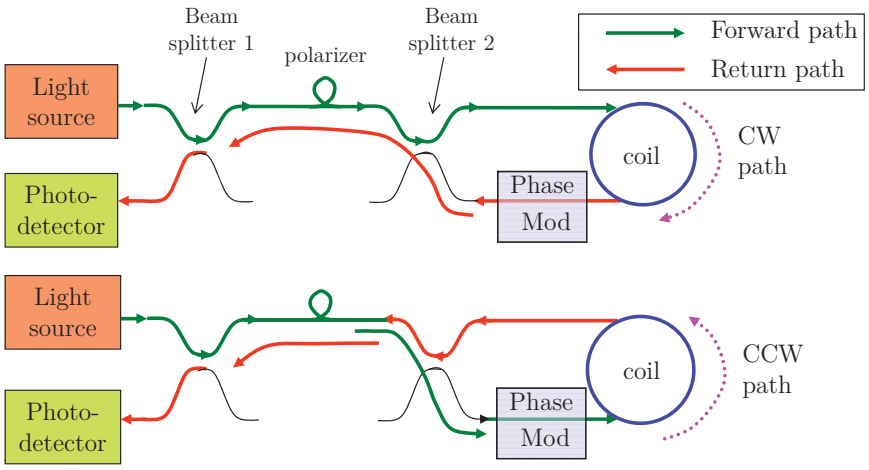

Figure 2.2: Reciprocal configuration of a FOG [19].

With the above parameters, the phase difference due to the earth's rotation is obtained as follows.

$$\Delta\phi = SF \cdot \Omega = 3.79 \cdot 10^{-5}\ rad \tag{2.11}$$

2.1.2 Reciprocity

According to [10], reciprocity states that for any optical wave in a linear medium, there is an opposite wave which propagates with exactly the same accumulated phase and the same attenuation. In a FOG, we use reciprocal configuration in order to ensure that phase shift between CW and CCW waves is due to rotation only. Thus, we force beams to follow identical paths [19]. The paths followed by beams in reciprocal configuration are shown in Figure 2.2. This configuration is also called as minimum configuration of FOG.

In this configuration, CW and CCW waves travel identical paths in opposite directions. 50 % of the wave from light source passes through the first beam

splitter. Then, polarized wave after polarizer passes through the second beam splitter. One of the output of second beam splitter passes through the fiber coil directly in CW direction. The CW wave enters phase modulator after the fiber coil. The CCW wave moves vise versa. In other words, the CCW wave first enters the phase modulator, then passes through the fiber coil. CW and CCW waves return back and interfere at the photodetector.

Nonreciprocal phase shift is relative phase shift between CW and CCW waves. In order to ensure that Sagnac effect is the only source of nonreciprocal phase, it is important to minimize nonreciprocal effects. The reasons and possible solutions for undesirable nonreciprocities are listed in [20] as follows:

- Polarization effects are taken care of by using polarization-maintaining (PM) fiber and placing a good polarizer in the path between two couplers,
- Back reflection or scattering is eliminated by the use of a broadband light source,
- Intensity-dependent nonlinear index changes, known as the optical Kerr effect, can be reduced by using a broadband light source,
- Time-dependent temperature gradient along the fiber that causes bias drift (Shupe effect) can be reduced by special fiber coil winding technique,
- External magnetic fields can be reduced by the use of magnetic shields,
- Electronic offset errors can be reduced by proper electronics design.

2.2 Optical Configuration of Fiber Optic Gyroscope

The main role of the optical scheme of a FOG is to produce a signal depending on rotation rate by the principle of Sagnac effect. Firstly, we established the optical

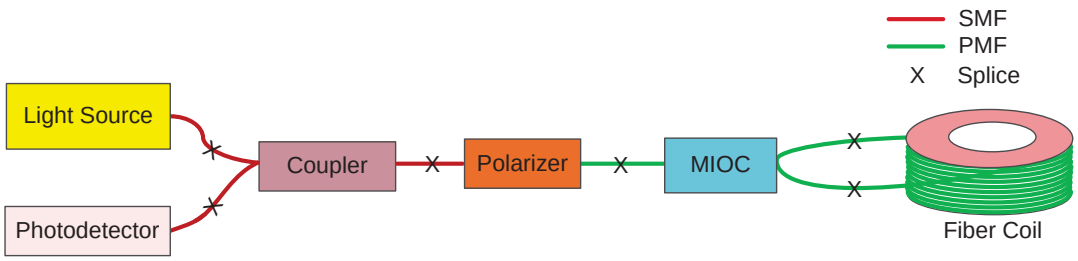

Figure 2.3: Optical configuration of the FOG.

scheme which consists of a broadband source, a coupler, a polarizer, a multifunctional integrated optical chip (MIOC) and a fiber coil. Light wave travels in the optical configuration starting from the light source. The photodetector detects returning light and rate signal is determined by using the detected signal. The detection scheme would be given in Chapter 4 in detail.

The optical configuration of the FOG is given in Figure 2.3. In the scheme, SMF refers to an ordinary single-mode fiber, i.e., non-polarization-maintaining fiber and PMF refers to polarization-maintaining single-mode fiber. As shown in this configuration, all components are fiber pigtailed and there are splice points between them. At each of the splice points, the ends of the fibers should stripped, cleaned, cleaved and spliced together by fusing them with heat. Finally, we recoats the splice point with a protective layer in order to prevent damage. We are using splicing tools such as stripper, cleaver, fusion splicer and recoater at the steps involved in fiber splicing.

The main difference between the minimum configuration and the configuration used in this work is a component called MIOC. This component behaves as both the second beam splitter and phase modulators. The optical scheme that contains a MIOC is the optimal configuration of FOG.

Fiber optic gyroscopes are designed to meet requirements of the systems. The number of axis is important for design criteria. Depending on its usage, FOGs are designed as single, two, three or more axis. The number of axis would directly

determine used components and their numbers. For instance, if one intends to use single light source for non-single-axis gyroscope, a beam splitter after light source is used commonly. In addition, the other components are used likewise for each axis.

The details regarding the components of the optical scheme of FOG are described at the rest of this section.

2.2.1 Fiber Coil

Fiber coil is the heart of Sagnac interferometer as phase difference due to rotation rate occurs in it. Sagnac effect and scale factor are dependent on fiber coil parameters which are its length and diameter. As length and diameter of the fiber coil increase, the sensitivity of FOG also increases.

A fiber coil made of stress-induced high-birefringence polarization-maintaining (PM) single-mode fiber gives the best performance in a FOG. In PM fiber, most of the power is maintained in the primary reciprocal waves, avoiding signal fading and a small part is transferred in the crossed nonreciprocal wave. Furthermore, the power in the crossed nonreciprocal wave gets depolarized since it propagates at a different velocity compared to the main mode, in the case of using a broadband source [10, 21].

Fiber coils should be carefully wound to minimize thermal and stress gradients, asymmetries and dynamic responses [19]. Shupe showed that the accuracy of the FOG can be limited by a thermally induced nonreciprocity caused by a time-dependent temperature gradient along the fiber coil [22]. This nonreciprocal error is known as Shupe effect. Symmetrical quadrupole winding is a widely used method in order to reduce Shupe effect. Moreover, low winding tension is used to minimize coil stress.

Faraday effect can also cause drift in a FOG. If the sensing loop was made of an ideal circular single-mode fiber, the Faraday effect would have been cancelled due to reciprocal configuration [23]. However, as retarders are situated at asymmetric

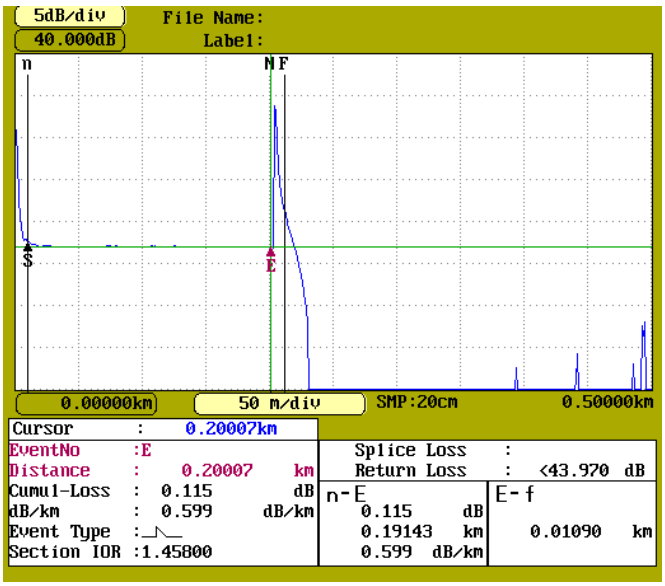

Figure 2.4: The measurement of the fiber coil's length with OTDR.

points due to twisting in the fiber coil, the phase difference appears due to the nonreciprocity of the Faraday effect [23, 24]. The Faraday effect is suppressed by using a polarization-maintaining fiber but not completely nulled out. For further improvement, shielding of the coil with permeability material such as μ-metal is necessary [10].

We have used a coil made of PM fiber with a length of 200 m in the optical configuration. The fiber coil was wound with symmetrical quadrupole winding method and shielded with μ-metal. The mean diameter of the coil is 28 mm. The fiber length is measured with optical time-domain reflectometer (OTDR). As seen in the Figure 2.4, the fiber length is 200 m.

2.2.2 Light Source

A light source produces light travelling in fiber optic gyroscopes. The stability of wavelength can be considered as one of the key performance specifications since scale factor is proportional to mean wavelength. The output power of light sources should be also adequate taking the required power falling onto photodetector, splitting of beam in two couplers (one is inside MIOC) twice and losses in optical

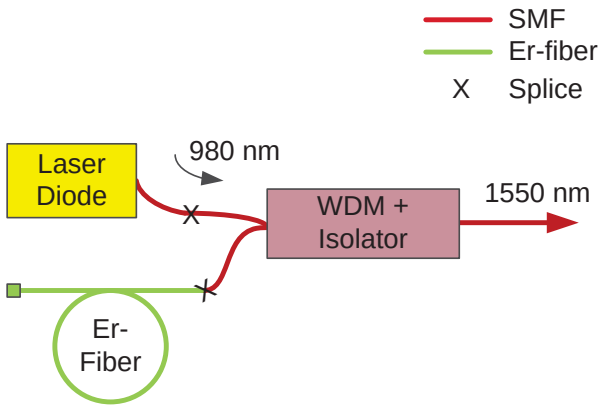

Figure 2.5: Configuration of the ASE light source.

path into account. Broadband sources give the best performance in the FOG since they eliminate optical Kerr effect and back reflection or scattering. Recently, two types of broadband light sources are used in FOGs: superluminescent diode (SLD) and the erbium-doped superfluorescent fiber source.

Erbium-doped fiber based amplified spontaneous emission (ASE) light source is chosen in the FOG design since it has several advantages over SLD technology such as high output power and wavelength stability over temperature. The ASE light source configuration is given in Figure 2.5.

In the light source, erbium-doped fiber is induced by a laser pump diode. The inverted ions produce a spontaneous emission, some of which is captured by the fiber core [25]. We have used a cooled laser diode since source wavelength changes can be reduced by temperature control. The wavelength of pump laser diode is chosen as 980 nm which is the absorption wavelength of erbium-doped fiber. The advantages of choosing 980 nm-wavelength is to be more up to date technology, the amount of power, low cost and ease of supply. For similar reasons, the wavelength of remaining optical components is chosen as 1550 nm.

The used configuration is known as backward configuration such that the signal comes out at the pump input. The pump is filtered out from the output by a wavelength division multiplexing (WDM) fiber coupler. Consequently, the light couples strongly over the bandwidth of the ASE, but minimally at the pump

wavelength. We used a hybrid component which contains a WDM coupler and an isolator. The isolator is used to reduce the sensitivity of mean wavelength to changes in feedback levels. Lower sensitivity to feedback is one of the advantages of the backward configuration over forward one [25]. The relative intensity noise and power efficiency are the other factors to prefer this configuration.

The center wavelength of the light source can be calculated by weighted average of power spectral density. It can be also called power-weighted mean wavelength and its formula is given as follows:

$$\langle \lambda \rangle = \frac{\int P(\lambda)\lambda d\lambda}{\int P(\lambda) d\lambda} \tag{2.12}$$

where $P(\lambda)$ is the power spectral density.

For complex-shaped spectrum, the spectral width is specified with root-mean-square deviation as given in Equation (2.13).

$$\Delta\lambda = \sqrt{\left| \frac{\int P(\lambda)\lambda^2 d\lambda}{\int P(\lambda) d\lambda} - \langle \lambda \rangle^2 \right|} \tag{2.13}$$

The spectrum of the light source is obtained by optical spectrum analyzer (OSA) and given in Figure 2.6. The center wavelength and the spectral width of the light source are found as 1537.3 nm and 11.4 nm, respectively.

A benchtop laser diode-thermoelectric cooling (TEC) controller is used to drive laser diode and control its temperature. We used the driver in constant current mode adjusting the required current to drive the laser diode.

2.2.3 Coupler

A coupler is used after the light source. The main function of the used coupler is to split the beam into two branches. In forward path, 50 % of the light from the light source is transferred to the polarizer. In backward path, 50 % of the returning

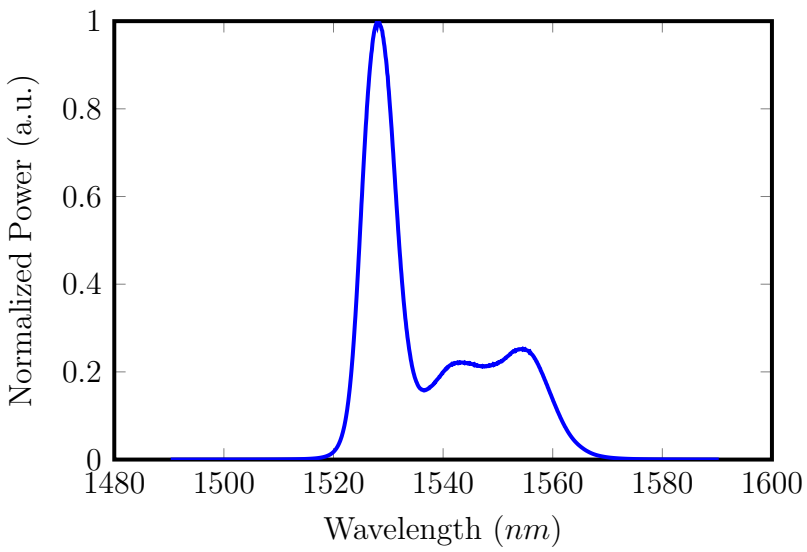

Figure 2.6: Optical spectrum of the light source.

light from the fiber coils is transferred to the photodetector. The coupler is named as 3 dB-coupler since the split ratio is 50:50 % ideally.

All-fiber coupler is desirable because it allows continuous mode guiding and there exists no loss at interface between fiber and bulk-optics [19].

2.2.4 Polarizer

Since we have used PM fiber in the fiber coil, the light should be polarized before entering the fiber coil. A polarizer is a component that converts unpolarized light into polarized light. Although the position of the polarizer is optional, putting it before the MIOC is the best solution in order to use minimum number of PM components. The polarizer guides only one state of polarization. There are a couple of techniques to polarize the light such as using an in-line polarizer and polarizing fiber. We have used an in-line polarizer which polarizes light with high extinction ratio.

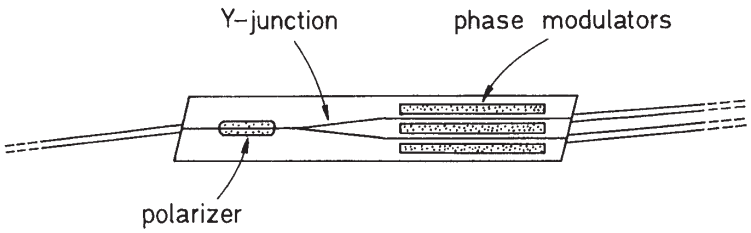

Figure 2.7: The structure of MIOC [10].

2.2.5 Multifunctional Integrated Optical Chip

Signal processing techniques which will be described in Chapter 3 in detail, allow to solve the nonlinearity problem of response of interferometer and get an accurate linearized measurement. Modulation of the optical-wave phase is the best-performing approach. Integrated optics have the unique advantage of making possible the fabrication of such broad-bandwidth phase modulators [10].

Multifunctional integrated optical chip (MIOC) is a hybrid component including a polarizer, a splitter/combiner and phase modulators. In MIOC, polarized light is split into two branches with equal power and then electric field would be created in both branches by means of electrodes inside MIOC. The index seen by the optical wave is changed by applying electric field. Optical waves that have the desired phase from each branch would enter to both ends of a fiber coil. The structure of MIOC is given in Figure 2.7.

A waveguide is fabricated by increasing the refraction index of the crystal underneath the surface that acts as the cladding of an optical fiber. The optimal choice for material of integrated optical chip is lithium niobate ($LiNbO_3$). The fabrication technique of waveguides is titanium (Ti) in-diffusion. The Y-junction is composed of a base single-mode waveguide connected to two single-mode branch waveguides. Light propagated in the waveguide is split equally into two branch waveguides diverged with a very small angle to minimize loss [10].

Chapter 3

Modulation and Demodulation Techniques in Fiber Optic Gyroscope

3.1 Interference Signal

A fiber optic gyroscope is a sensor that uses the interference of light to detect rotation rate. A FOG measures phase difference between two lights propagating in opposite directions in fiber loop, due to the rotation. The signal with the information of Sagnac phase difference ($\Delta\phi_R$) is received by the photodetector and output signal is generated. The relation between the intensity and the phase difference based on the principle of interference is given in Equation (3.1).

$$I = \frac{I_0}{2}\left[1 + \cos(\Delta\phi_R)\right] \tag{3.1}$$

Interference signal dependent on phase difference is shown in Figure 3.1. If there exists no rotation, I equals to I_0, i.e., maximum photocurrent. Ignoring the sign of derivative, the sensitivity of interference signal is given as:

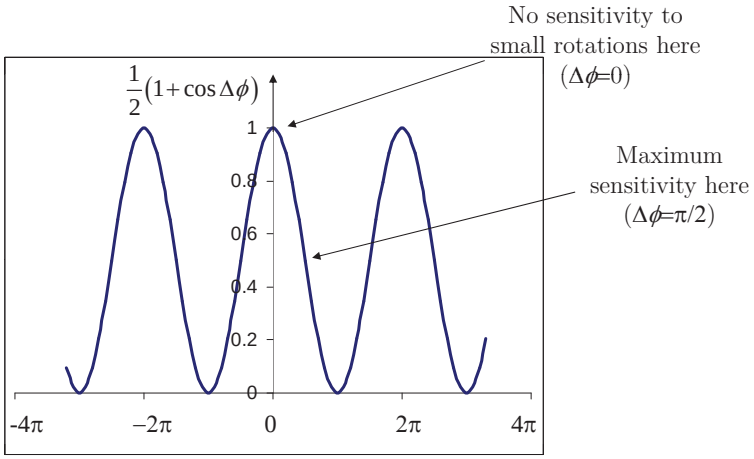

Figure 3.1: Interference signal [19].

$$\frac{\partial I}{\partial \Delta\phi_R} = \frac{I_0}{2}\sin(\Delta\phi_R) \tag{3.2}$$

While the phase difference is around zero ($\Delta\phi_R \approx 0$), the sensitivity is at the lowest level. In this case, it is not possible to predict even the direction of rotation. There are several modulation techniques to linearize the response of interferometer. While modulation signal is applied to the MIOC, the signal obtained from the photodetector should be demodulated by signal-processing methods. Rotation rate signal is the output of digital detection and processing systems. The signals in a FOG is shown in Figure 3.2.

3.2 Square-wave Bias Modulation Technique in FOG

Square-wave bias modulation is widely-used technique in high-performance FOGs. In order to create a permanent phase difference between two counter-propagating light waves, $\pi/2$ phase shift can be applied. Thus, interference signal behaves as sinus function and sensitivity would be at the highest level at zero

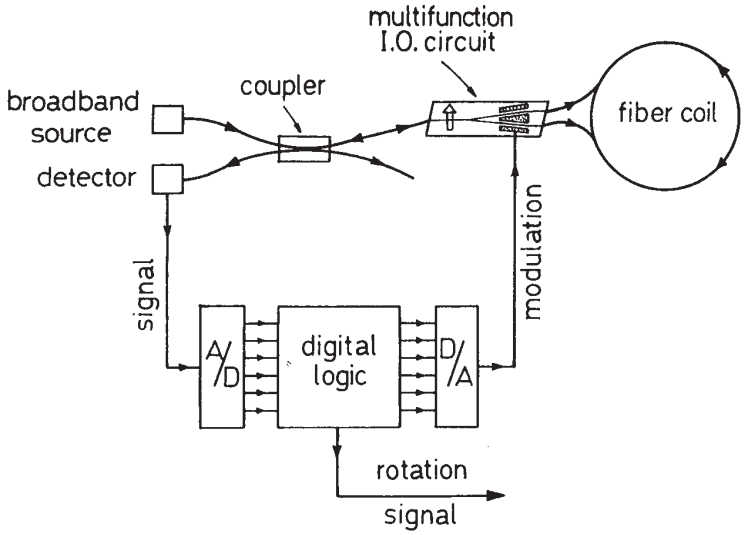

Figure 3.2: The configuration of a FOG with photodetection, modulation and rotation rate signals [10].

point. Equations (3.3) and (3.4) give the interference signal in case of square-wave bias modulation.

$$I = \frac{I_0}{2}[1 + \cos(\Delta\phi_R + \Delta\phi_m)] \tag{3.3}$$

$$\Delta\phi_m = \frac{\pi}{2} \Rightarrow I = \frac{I_0}{2}[1 + \sin(\Delta\phi_R)] \tag{3.4}$$

It is necessary to place a phase modulator (or an integrated optical chip with phase modulators) before/after the fiber coil. When a certain voltage is applied to the phase modulator, it applies a phase shift due to refractive index change. The details of operational principle of a phase modulator are described in Chapter 2. The modulation phase due to applied voltage can be expressed in Equation (3.5) where K is the phase modulation constant and $V(t)$ is the voltage applied to the phase modulator.

$$\phi_m(t) = KV(t) \tag{3.5}$$

Thinking the minimum reciprocal configuration, while wave in the CCW direction enters the phase modulator without passing through the fiber coil, wave

in the CW direction passes through the phase modulator after the fiber coil. A fiber coil acts as a retardant and creates a delay of τ which is defined as transit time. The transit time of the light through the coil, τ, is dependent on the length of fiber coil (L) and the refractive index of fiber (n). τ can be found via the formula in Equation (3.6).

$$\tau = \frac{nL}{c} \tag{3.6}$$

As an example; the transit time for 200 m fiber with a refractive index of 1.5 can be calculated as:

$$\tau = \frac{1.5 \cdot 200\ m}{3 \cdot 10^8\ m/s} = 1\ \mu s \tag{3.7}$$

Due to the delay in fiber coil, while the CW wave passes through the phase modulator at time t, the CCW wave passes at time $t - \tau$. The phase difference due to the phase modulation in a FOG can be expressed as:

$$\Delta\phi_m(t) = K[V(t) - V(t - \tau)] \tag{3.8}$$

Equation (3.8) can be revised as:

$$\Delta\phi_m(t) = \phi_m(t) - \phi_m(t - \tau) \tag{3.9}$$

The signals falling onto the photodetector in the cases of 'no rotation' and 'finite rotation' are shown in Figure 3.3, while square-wave modulation is applied to the phase modulator. Square-wave makes transitions at two points of interference signal in time. During these transitions, spikes in the photodetector signal occur.

The screenshots of the output and modulation signals captured from oscilloscope in the cases of absence and presence of rotation are given in Figure 3.4.

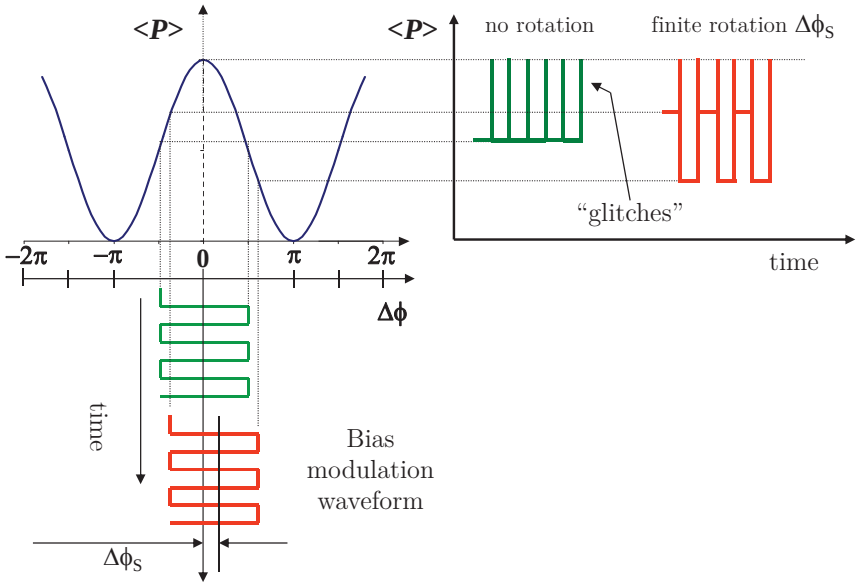

Figure 3.3: Photodetector signals with and without rotation when square-wave bias modulation is applied [19].

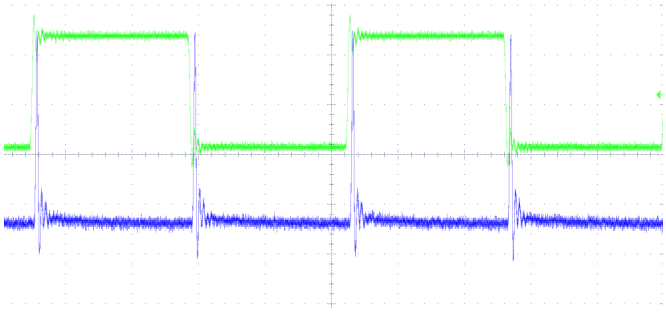

(a) No rotation.

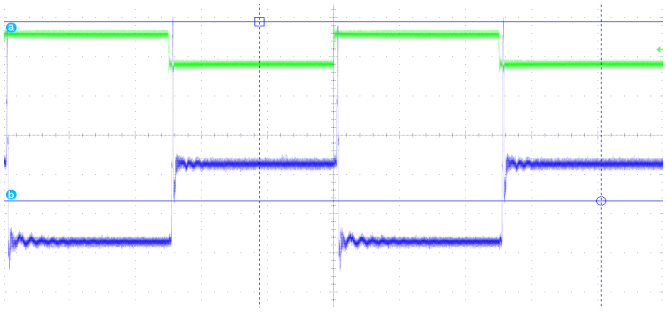

(b) Finite rotation.

Figure 3.4: The output (*blue*) and modulation (*green*) signals in the cases of absence and presence of rotation.

The period of square-wave is twice of transit time, 2τ. The modulation frequency corresponds to the so-called *proper* (or *eigen*) frequency. Proper frequency can found as:

$$f_p = \frac{1}{2\tau} = \frac{c}{2L} \tag{3.10}$$

In order to crete $\pi/2$ phase difference between the waves, $\phi_m(t)$ should be applied to phase modulators. The modulation phases for CW and CCW waves are $\phi_m(t)$ and $\phi_m(t-\tau)$ as given in Equations (3.11).

$$\phi_m(t) = \begin{cases} +\frac{\pi}{4}, & 2i\tau \leq t < (2i+1)\tau; \\ -\frac{\pi}{4}, & (2i+1)\tau \leq t < (2i+2)\tau. \end{cases} \tag{3.11a}$$

$$\phi_m(t-\tau) = \begin{cases} +\frac{\pi}{4}, & (2i+1)\tau \leq t < (2i+2)\tau; \\ -\frac{\pi}{4}, & 2i\tau \leq t < (2i+1)\tau. \end{cases} \tag{3.11b}$$

Then, by using Equation (3.9), the phase difference between the counter propagating waves can be found:

$$\Delta\phi_m(t) = \begin{cases} +\frac{\pi}{2}, & 2i\tau \leq t < (2i+1)\tau; \\ -\frac{\pi}{2}, & (2i+1)\tau \leq t < (2i+2)\tau. \end{cases} \tag{3.12}$$

3.3 Demodulation Techniques in FOG

After detection of the output signal by a photodetector, demodulation process should be performed. During the period of the system (2τ), the signals in the first and second τ semi-periods are defined as *odd* and *even* signals, respectively.

When square-wave bias modulation is applied to the system, interference signal becomes that given in Equations (3.13) for two different portions of the signal.

$$I_{odd} = \frac{I_0}{2}[1 + \cos(\Delta\phi_R + \Delta\phi_m)] \tag{3.13a}$$

$$I_{even} = \frac{I_0}{2}[1 + \cos(\Delta\phi_R - \Delta\phi_m)] \tag{3.13b}$$

$\Delta\phi_R$ can be obtained in terms of $\Delta\phi_m$, I_{even} and I_{odd}. Starting point to obtain $\Delta\phi_R$ is to find the difference between I_{even} and I_{odd}:

$$I_{even} - I_{odd} = \frac{I_0}{2}[\cos(\Delta\phi_R - \Delta\phi_m) - \cos(\Delta\phi_R + \Delta\phi_m)] \tag{3.14}$$

We find $\Delta\phi_R$ defining $I_{even} - I_{odd}$ as ΔI.

$$\Delta I = I_0 \sin(\Delta\phi_R)\sin(\Delta\phi_m) \tag{3.15}$$

$$\Delta\phi_R = \arcsin\left(\frac{\Delta I}{I_0 \sin(\Delta\phi_m)}\right) \tag{3.16}$$

By small angle approximation,

$$\Delta\phi_R \approx \frac{\Delta I}{I_0 \sin(\Delta\phi_m)} \tag{3.17}$$

Eliminating I_0 from rotation rate equation is important since it is necessary to know maximum photocurrent of the system to calculate $\Delta\phi_R$. Although it is easy to find the maximum photocurrent, power can fluctuate in time and this problem would directly effects rotation rate measurements. Starting from summation of I_{even} and I_{odd}, we can obtain I_0.

$$I_{even} + I_{odd} = \frac{I_0}{2}[2 + \cos(\Delta\phi_R - \Delta\phi_m) + \cos(\Delta\phi_R + \Delta\phi_m)] \tag{3.18}$$

We find $\Delta\phi_R$ defining $I_{even} + I_{odd}$ as ΣI.

$$\Sigma I = I_0[1 + \cos(\Delta\phi_R)\cos(\Delta\phi_m)] \tag{3.19}$$

For small $\Delta\phi_R$, I_0 can be found as:

$$\Sigma I \approx I_0[1 + \cos(\Delta\phi_m)] \tag{3.20}$$

$$I_0 \approx \frac{\Sigma I}{1 + \cos(\Delta\phi_m)} \tag{3.21}$$

Substituting Equation (3.21) into Equation (3.16), $\Delta\phi_R$ can be found.

$$\Delta\phi_R \approx \arcsin\left(\frac{\Delta I}{\Sigma I} \cdot \frac{1 + \cos(\Delta\phi_m)}{\sin(\Delta\phi_m)}\right) \tag{3.22}$$

One of the advantages of $\pi/2$ square-wave bias modulation is that it is not necessary to make an assumption of small $\Delta\phi_R$. Therefore, the function to calculate $\Delta\phi_R$ is valid for all rotation rates. Rewriting of Equation (3.19) in this condition is given Equation (3.23).

$$\Delta\phi_m = \frac{\pi}{2} \Rightarrow \Sigma I = I_0 \tag{3.23}$$

Using Equations (3.15), (3.16)and (3.23), $\Delta\phi_R$ can easily found for the case of $\pi/2$ square-wave bias modulation.

$$\Delta\phi_m = \frac{\pi}{2} \Rightarrow \Delta I = I_0 \sin(\Delta\phi_R) \tag{3.24}$$

$$\Delta I = \Sigma I \sin(\Delta\phi_R) \tag{3.25}$$

$$\Delta\phi_R = \arcsin\left(\frac{\Delta I}{\Sigma I}\right) \tag{3.26}$$

As it can be seen in Equation (3.26), in case of $\pi/2$ square-wave bias modulation, phase difference due to the rotation rate equals 'arcsin' function of the ratio of difference to summation of even and odd signals. 'arcsin' function function goes linear region when phase difference converges to zero. Thus, Equation (3.26) can be directly expressed as the ratio of the difference to summation of even and odd signals.

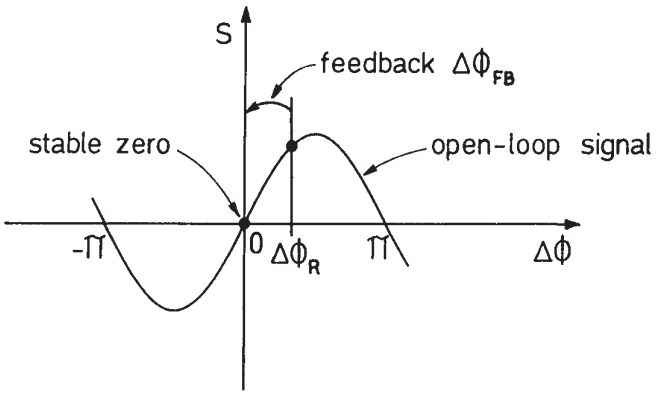

Figure 3.5: Feedback algorithm in closed loop FOG [10].

3.4 Closed Loop Fiber Optic Gyroscope

Square-wave bias modulation scheme may be insufficient to provide sensitivity at all dynamic ranges, while providing a good stability around 'zero'. In order to achieve strong linearity, the operating point should be controlled around 'zero'. This problem can be solved with closed loop scheme.

In the closed loop algorithm, demodulated signal, in other words, open loop signal, is used as error signal and it feeds back into the system. The feedback phase shift ($\Delta\phi_{FB}$) equals Sagnac phase shift ($\Delta\phi_R$) and its sign is opposite (See Figure 3.5). So the phase shift in closed loop FOG can be expressed as the total of Sagnac, feedback and modulation phase shifts as given in Equation (3.27).

$$\Delta\phi = \Delta\phi_R + \Delta\phi_{FB} + \Delta\phi_m \tag{3.27}$$

The relation between the output signal of FOG and total phase shift is given in Equation (3.28). As $\Delta\phi_{FB}$ cancels $\Delta\phi_R$, phase difference would be zero and interference signal would depend on only modulation phase shift.

$$I = \frac{I_0}{2}[1 + \cos(\Delta\phi_R + \Delta\phi_{FB} + \Delta\phi_m)] \tag{3.28}$$

$$\Delta\phi_{FB} = -\Delta\phi_R \Rightarrow I = \frac{I_0}{2}[1 + \cos(\Delta\phi_m)] \tag{3.29}$$

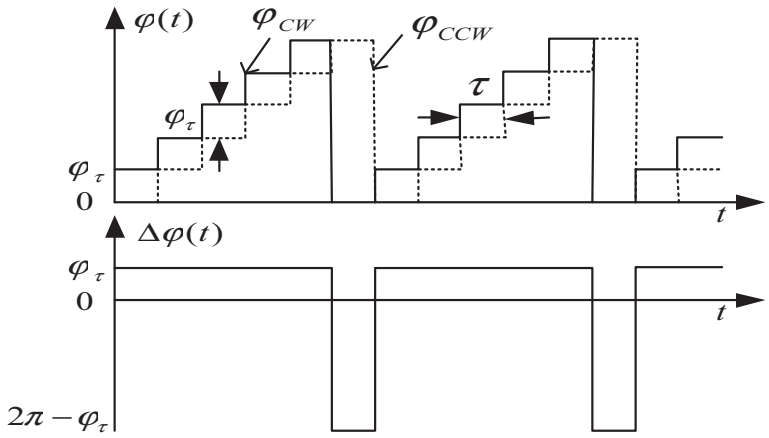

Figure 3.6: Digital phase ramp signal in closed loop FOG [15].

The feedback signal is also applied to the phase modulator (or integrated optical chip with phase modulators) as that in the case of bias modulation signal. The most common method for feedback signal is applying digital phase ramp signal. A constant rotation rate would create the phase ramps with constant steps. The phase difference between counter-propagating waves would compensate with $\Delta\phi_{FB}$. Due to the position of phase modulator, digital phase ramp signal applied to the CCW wave is delayed with respect to that applied to the CW wave. The application method of digital phase ramp is shown in Figure 3.6. As it can be observed from the figure, the relation between ϕ_{cw} and ϕ_{ccw} is given as:

$$\phi_{ccw}(t) = \phi_{cw}(t - \tau) \tag{3.30}$$

The feedback phase difference would be:

$$\Delta\phi_{FB} = \phi_{cw}(t) - \phi_{ccw}(t) \tag{3.31}$$

$$\Delta\phi_{FB} = \phi_{FB}(t) - \phi_{FB}(t - \tau) \tag{3.32}$$

where $\phi_{FB}(t)$ equals to $\phi_{cw}(t)$.

The difference between open and closed loop algorithms is shown in Figure 3.7. Square-wave bias modulation signal is same for both schemes. In closed loop

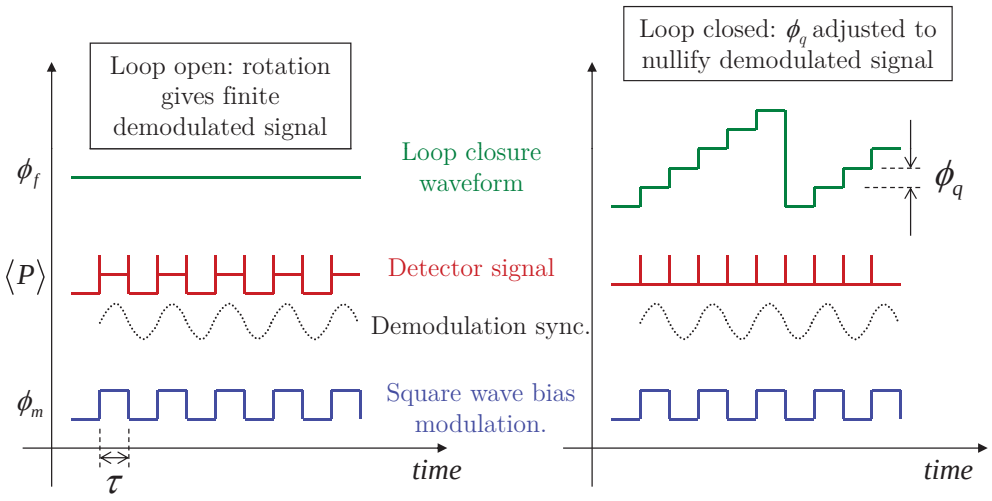

Figure 3.7: Digital phase ramp, photodetector and square-wave modulation signals in open and closed loop FOGs [19].

scheme, due to the phase ramp signal (feedback signal), the signal fall onto the photodetector is almost a constant signal. Spikes occur in both schemes due to the square-wave bias modulation signal.

It is impossible to create a phase ramp signal with infinite steps in one (positive or negative) direction because of the limitation of dynamic ranges of electronic components. Resetting is necessary after overflow to cope this problem. Since the interference signal is a periodic signal with 2π, the difference between pre-reset and post-reset values should be 2π. Figure 3.8 presents resetting process of the signal obtained by summation of square-wave bias modulation and phase ramp signals.

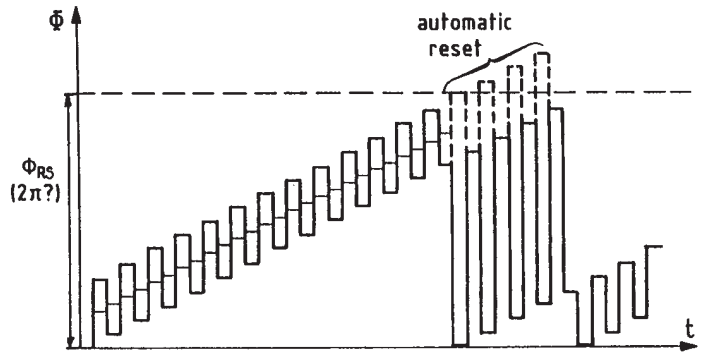

Figure 3.8: Resetting process in closed loop scheme [10].

3.5 Analog Approach for Preprocess Before Demodulation

The photodetector signal is noisy and contains spikes in transit time (τ) period due to the square-wave bias modulation. In addition, it is a current signal and needed to convert into voltage. Therefore, FOG electronics contains a transimpedance amplifier (TIA) that converts current signal into voltage and amplifies it. In order to increase the dynamic range of TIA circuit, DC signal can be subtracted from the original photodetector signal via a feedback loop. In this case, DC signal should be read by another circuit to monitor the changes in total power.

Furthermore, undesirable spikes can be eliminated with an analog switch circuit before entering into the A/D (analog-to-digital) converter. Analog switch is controlled by a gate signal which is a pulse signal with a duty cycle determined by spike width. The gate signal makes the analog switch on and off in τ period. It allows spike-free signal and eliminates spiky portion of the signal. After analog switch circuit, there can exist an integration circuit to integrate spike-free signal in τ period. Actually, the total integration time is not τ anymore, but lower than τ. However, the time between the start times of integration is exactly τ. In Figures 3.9 and 3.10, the spike-free signal after the switch circuit and the integrated signal captured from oscilloscope are shown.

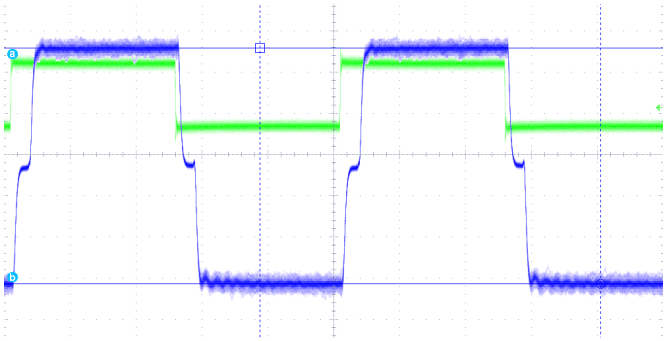

Figure 3.9: Spike-free signal obtained after analog switch circuit.

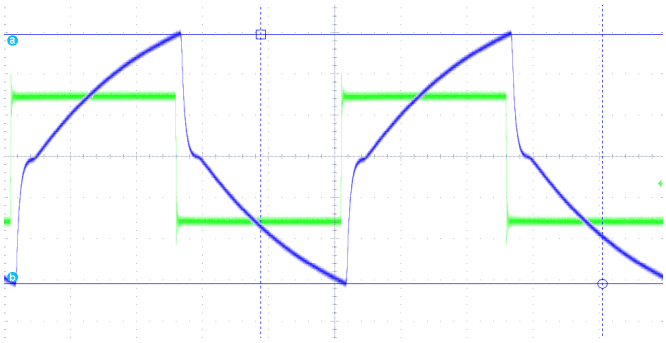

Figure 3.10: Integrated signal in every τ period.

After integration circuit, the signal enters an A/D convertor. The convertor samples the signal at the end of each integration period. The sample rate of the A/D convertor should be chosen adequately such that it receives at least one sample in the transit time, τ. For example for a FOG with 200 m fiber coil, the sample rate of the A/D convertor should be at least about 1 $^{\text{MS}}/_{\text{s}}$. All the subsequent operations are performed digitally by a processor after A/D conversion process.

Chapter 4

Digital Detection System of Fiber Optic Gyroscope

4.1 Configuration of Digital Detection System

The digital detection scheme of the FOG is described in this chapter. The modulation and demodulation algorithms are performed via a digital processor and rotation rate is given as an output of the signal processing unit. Moreover, a digital approach for preprocess before demodulation is presented as an alternative to analog approach details of which described in Section 3.5.

Detection process of the FOG consists of travelling of the signals in the fiber coil, phase modulation, photodetection, preamplification, A/D (analog-to-digital) conversion, digital demodulation and D/A (digital-to-analog) conversion.

A benchtop data acquisition (DAQ) system is built in order to develop necessary algorithms and processes. The configuration of the digital detection system is shown in Figure 4.1. The system gives rotation rate as an output signal. The whole system contains the following hardware items:

1. Photodetector: detects the optical signal and converts to the current signal.

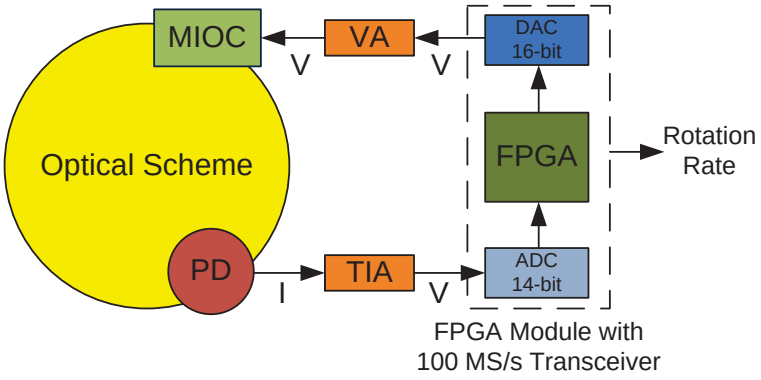

Figure 4.1: Configuration of the digital detection system.

2. TIA: converts current signal into voltage signal and amplifies it.

3. A/D convertor: converts the output of TIA into digital form.

4. FPGA processor: demodulates the digital signal and gives the rotation rate as the output of FOG.

5. D/A convertor: converts the digital output of FPGA processor into analog format and gives the analog signal to modulate phase modulator (or integrated circuit that contains phase modulators).

6. Voltage amplifier: amplifies the output of D/A convertor to the required modulation signal level.

A PXI (**P**eripheral component interconnect e**X**tensions for **I**nstruments) system provided from the company National Instruments, has been established. PXI systems are computer-based, high-performance measurement and automation systems. The PXI system contains a chassis, a controller and an FPGA (field programmable gate array) module with a transceiver adapter module. The picture of the PXI system given in Figure 4.2.

Figure 4.2: PXI system included a chassis, a controller and an FPGA module with a transceiver adapter module.

4.1.1 Photodetector

The photodetector of the system should be chosen carefully not to degrade the performance of the FOG. Semiconductor PIN photodiodes are ideal because of their very high quantum efficiency. A ready-to-use, high speed InGaAs photodetector with fiber connector/physical contact (FC/PC) connectorized is used to detect the output optical signal. InGaAs photodetectors are suitable for our application because of its low dark current, speed and working wavelength. The responsivity of the detector is given as 0.95, which is very close to 1 [26].

4.1.2 Transimpedance Amplifier

The output of photodetector is a weak current signal so it should be converted to voltage and amplified. Transimpedance amplifier (TIA) is used for this purpose.

The considerations while choosing TIA can be listed as follows:

- TIA should be low noise.

- The gain of TIA should be compatible with the maximum input voltage of the A/D convertor and the output of photodetector.
- Working bandwidth should be DC to wideband (in the order of MHz).
- The input bias current should be low (lower than 1 nA is desirable).

Used TIA is variable-gain and high speed. For different gain parameters, it can be used in 'low noise' and 'high speed' options. When low-noise-option is preferred, gain is switchable from 10^2 to 10^7 $^V/_A$. However, as the bandwidth is inversely proportional to gain, TIA is not proper to use for higher gains. For example, while the bandwidth is 200 MHz for 10^2 $^V/_A$ -gain, it reduces to 220 kHz for 10^7 $^V/_A$ -gain.

As we have used a 200 m fiber coil, we need to apply approximately 500 kHz square-wave signal to the MIOC. According to conducted experiments and existing theories, for 500 kHz square-wave signal, the detection bandwidth should be at least 5 MHz. The main problem caused by lower bandwidth is bias on rotation rate. The spike signal expands on the proper portion of the signal that would be used for obtaining the rotation rate. Because of the fact that, the proper gains for low noise option are 10^2, 10^3 and 10^4 $^V/_A$ with the upper cut-off frequencies 200 MHz, 80 MHz and 14 MHz, respectively. Fortunately, for these gain values, the bandwidth is also switchable to 1 MHz and 10 MHz. In order to obtain reliable results for different gains, 10 MHz-bandwidth is chosen. Besides, there is a low-pass filter with 40 MHz cut-off frequency before A/D converter in the transceiver module. Therefore, the bandwidth above 40 MHz does not provide any advantage.

The output voltage swing of TIA is ± 1 V for linear amplification. Therefore, gain values for different inputs should be chosen accordingly. Fortunately, TIA and A/D converter is totally compatible in terms of their output-input ranges.

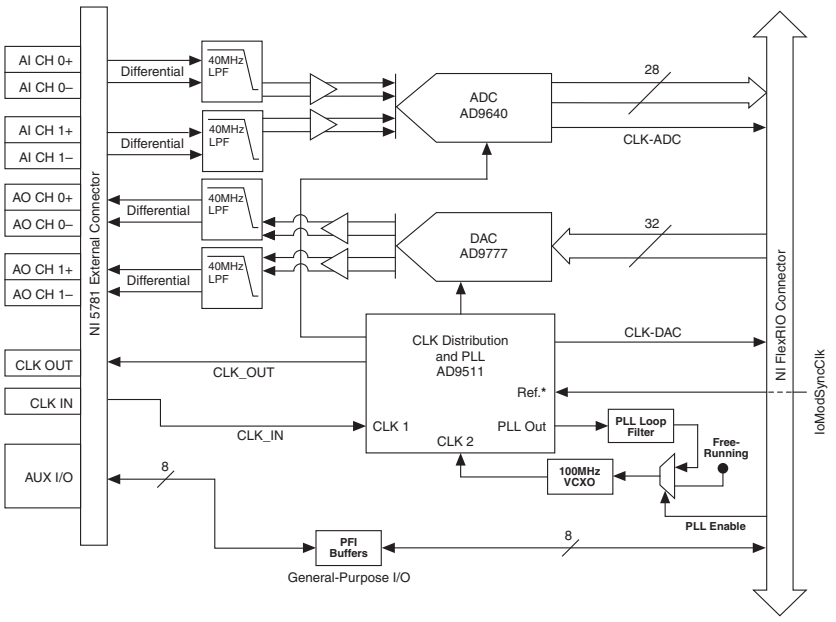

Figure 4.3: Block diagram of the transceiver adapter module [27].

4.1.3 A/D and D/A Conversion

After analog signal is converted into digital, a set of algorithms is performed in order to obtain rotation rate as an output. An FPGA module is used for this purpose. The FPGA module is integrated with a transceiver adapter module that contains an A/D convertor and a D/A convertor. Block diagram of the transceiver adapter module is shown in Figure 4.3.

The resolution of A/D convertor is 14-bit and the sampling rate of it is 100 MS/s. As Lefèvre gives an analysis in [10], 11 bits are sufficient to convert the analog signal without any dead band zone for 10^{-6} $rad/\sqrt{Hz}$. As noise analysis is performed in Chapter 5, the noise for our FOG system is in similar order of magnitude. Consequently, 14-bit-resolution is good enough for A/D conversion.

One of the advantages of A/D converter is its high sampling rate. The convertor allows to take more samples in a single semi-period. It means that in a 1 μs-period, 100 samples can be taken. Spike-free signal can be obtained by discarding some of the samples. The transactions such as analog switching and

integration can be performed digitally by the assistance of high sample rate. Digital integration of spike-free signal increases the performance in terms of noise.

The resolution of D/A convertor is 16-bit and the output update rate is 100 MS/s. For open loop systems, the duty of D/A converter is to create bias modulation signal. On the other hand, the D/A converter creates a feedback signal dependent on rotation rate in addition to bias modulation signal in closed loop systems. Especially for higher grade closed loop fiber optic gyroscopes, higher bit resolution should be necessary to increase the accuracy. However, in open loop systems as our system, a bit resolution value needed for A/D converter is also sufficient for D/A converter.

The frequency of modulation signal (proper frequency) directly depends on the fiber coil length as explained in Section 3.2. If the refractive index of fiber is taken as 1.5, one meter fiber creates approximately 5 ns delay in signal. As the output update rate of D/A converter is 100 M/S, it takes a sample in every 10 ns. Therefore, with the selected D/A converter, proper frequency can be adjusted approximately by the resolution of 2 m fiber length. The output update rate is important for the performance of the system. Improper frequency increases the width of spike and it causes deterioration of original signal and bias eventually. Moreover, identical sampling/update rate of A/D and D/A convertors makes coding related to time intervals in software easier. Another important parameter for D/A converter is its output settling time that is time required to reach and remain its final output value within a specified error band. It is given as 11 ns [28] which is good enough.

The output range of transceiver is actually 1 V_{pp}. However, V_π of a typical MIOC is in the range of 3 to 6 V. A voltage amplifier is used to amplify the output voltage of transceiver. The output range of the MIOC driver should be at least V_π of the MIOC to measure V_π value reliably. Similar requirements such as low noise and proper bandwidth are also valid for the voltage amplifier.

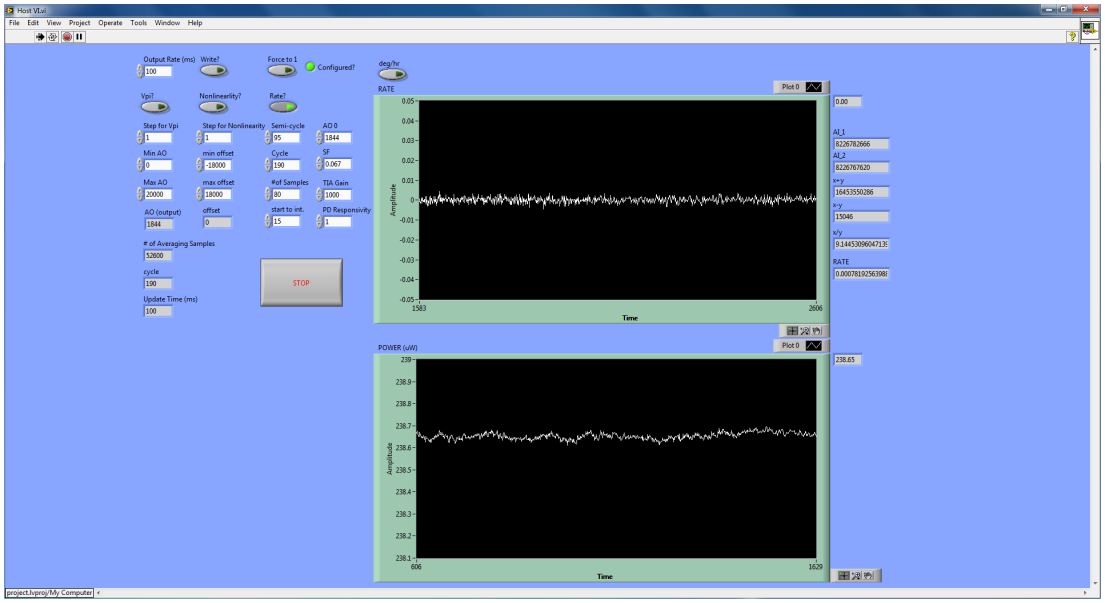

Figure 4.4: The user-interface implemented in LabVIEW environment.

4.2 Implementation of the Software

All digital signal processing algorithms has been implemented in the LabVIEW FPGA Module environment. The user-interface has been created in LabVIEW environment. LabVIEW offers a powerful graphical and user-friendly programming. The user-interface of the program is shown in Figure 4.4. Modulation and demodulation algorithms described in Chapter 3, are implemented to obtain rotation rate. The program allows us to monitor and log both the rotation rate and the power of the system.

4.3 Fundamental Experiments

4.3.1 Scale Factor Measurements

There is a single-axis rate and position table in NANOTAM. This table works as a rotation rate simulator. It is used in order to find scale factor and measuring range of the FOG. Moreover, we can use it with different rotation rates to calculate

Figure 4.5: Single-axis rate and position table in NANOTAM.

various errors in FOG such as bias error and scale factor error. The picture of single-axis rate simulator is given in Figure 4.5.

4.3.2 Characterization of the Phase Modulators

One of the important parameters of a phase modulator is its π voltage, V_π that is required voltage to produce a phase shift of π rad. In other words, if one applies voltage with an amplitude of V_π to the phase modulator, it creates π phase shift. V_π can be found by the principle of interference signal. As increasing the voltage applied to phase modulator, output data of the photodetector is monitored. Then, the interference equation is fitted to the data. π voltage is the corresponding applied voltage when we observe the minimum intensity at the output, first time. Figure 4.6 shows the graph obtained from V_π measurement.

Fringe visibility is a parameter that measures the strength of the interference and can be found as given in [29]:

$$V = \frac{I_{max} - I_{min}}{I_{max} + I_{min}} \tag{4.1}$$

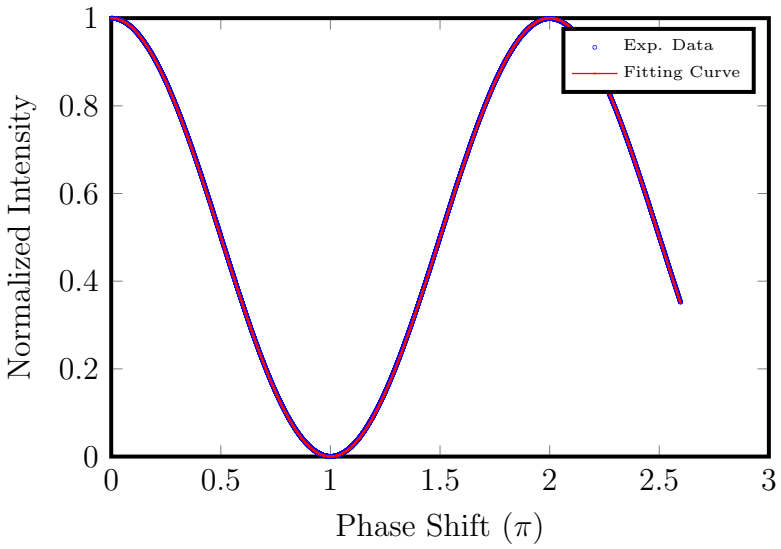

Figure 4.6: Intensity vs. phase shift.

Ideally, the fringe visibility is 1. As it decreases, bias of the FOG increases accordingly. Therefore, we need to obtain higher fringe visibility in order to get a good bias performance. Fortunately, we obtained 99.6 % fringe visibility from the above measurement, which is good enough.

4.3.3 Rotation Rate Measurements and Allan Variance Method

The most important parameters that determine the performance of FOG are angle random walk noise and bias instability. Bias instability refers to drift in the long term on non-random deviation on bias. Figure 4.7 illustrates the difference between noise and bias instability.

Allan variance method is used to provide a noise analysis and determine the performance parameters in FOGs (substantially all kinds of accelerometers and gyroscopes). The method is based on the Allan variance of the clusters with different amount of data obtained in long-term (for hours). The algorithm is as follows.

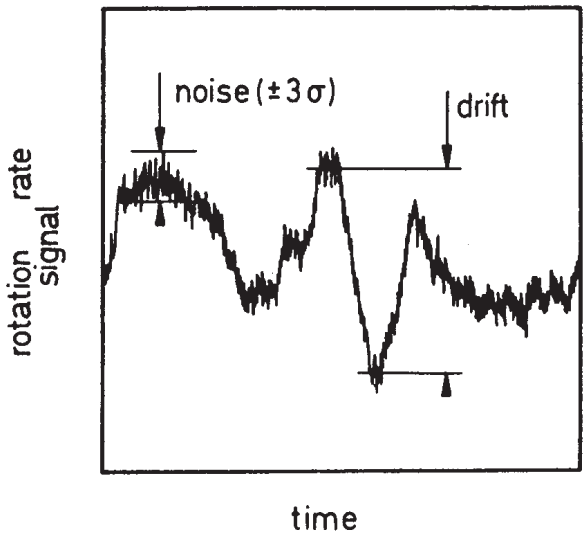

Figure 4.7: Drift and noise in rotation rate data [10].

1. Consider N samples of gyro data Ω with a sample time of τ_0.
   $t = k\tau_0, k = 1, 2, 3, ..., N$.

2. Form data clusters of lengths τ_0, $2\tau_0$,..., $k\tau_0$ ($k < N/2$).

3. Obtain averages of the sum of the data points contained in each cluster over the length of that cluster. The average rate between times t_k and $t_k + \tau$ is $\overline{\Omega}_k(\tau)$ where $\tau = m\tau_0$.

4. The Allan variance is defined as a function of cluster time and given in Equation (4.2) where $\langle\rangle$ is the ensemble average.

$$\sigma^2(\tau) = \frac{1}{2}\left\langle \left(\overline{\Omega}_{k+m} - \overline{\Omega}_k\right)^2 \right\rangle \tag{4.2}$$

5. The Allan variance is estimated as:

$$\sigma^2(\tau) = \frac{1}{2(N-m)} \sum_{k=1}^{N-m} \left(\overline{\Omega}_{k+m} - \overline{\Omega}_k\right)^2 \tag{4.3}$$

The most important aspect of Allan variance method is to analyze all types of noise and to be able to determine sources of the error. The standard document, "IEEE Standard Specification Format Guide and Test Procedure for Single-Axis Interferometric Fiber Optic Gyros" [30] is used for noise analysis in FOGs.

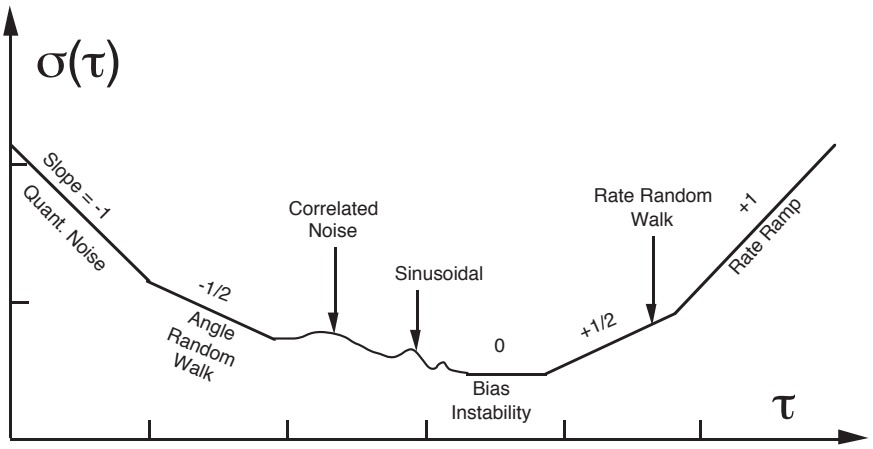

Figure 4.8: Noise types for fiber optic gyroscopes defined in IEEE Standards [30].

Figure (4.8) shows different noise components of FOG on Allan variance curve according to IEEE standards. Averaging over different time intervals, different noise processes with different slopes of curve can be identified. Although the curve is known as Allan variance, usually the deviation of the data, in other words, square root of the variance is plotted on a log-log graph.

During this work, Allan variance method is used for the analysis of data obtained from the FOG. We make measurements of rotation rate and apply Allan variance method. Figure 4.9 presents rotation rate data obtained without external rotation, i.e., with earth's rotation only. The data is taken in 1 Hz for 12 hrs.

Allan variance curve of the rotation rate data mentioned above is given in Figure 4.10. As it can be observed, the system has no quantization noise component. Furthermore, the apparent regions of the graph are angle random walk (ARW) and bias instability. To see the rest of the noise regions on graph, it may require to collect data for weeks. Fortunately, the main performance parameters are ARW and bias instability for a fiber optic gyroscope (substantially all kinds of accelerometers and gyroscopes). The detailed noise analysis will be given in Chapter 5.

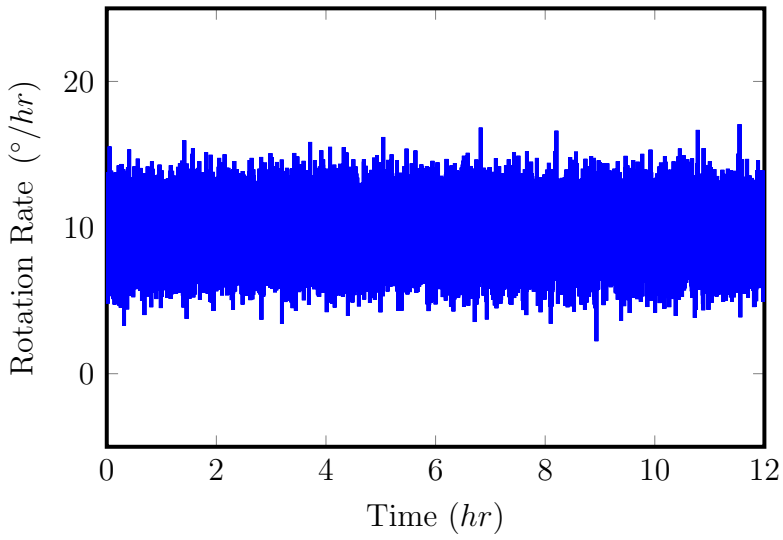

Figure 4.9: Earth's rotation rate measurement for 12 hrs.

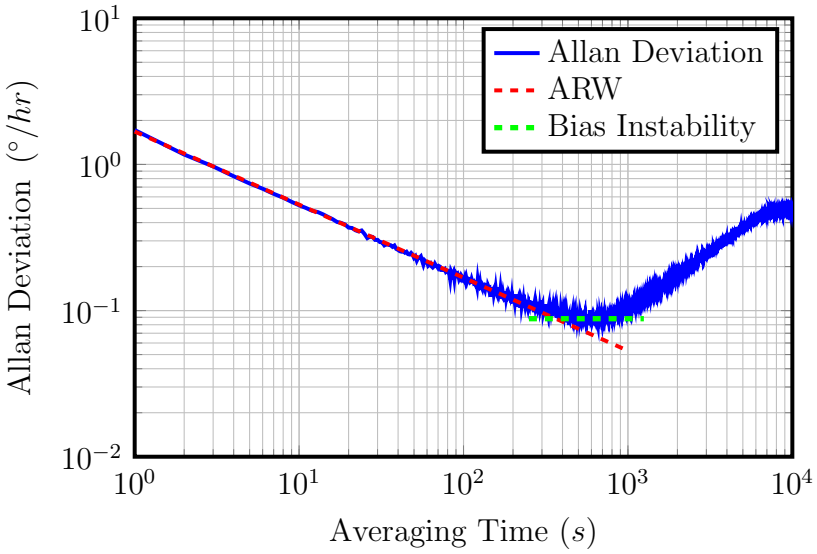

Figure 4.10: Allan variance curve.

ARW can be expressed as white noise component of total noise in a FOG. The source for this error is spontaneous emission of photons and other high frequency noise terms that have correlation time much shorter than sample time [30]. The slope of ARW in the log-log plot of Allan deviation is $-1/2$. ARW (N) can be found using Equations (4.4) and 4.5. The widely used unit for ARW is $^\circ/\sqrt{hr}$.

$$\sigma^2(\tau) = \frac{N^2}{\tau} \tag{4.4}$$

$$N = \sigma(\tau)\sqrt{\tau} \tag{4.5}$$

Bias instability is a kind of drift in the data due to bias fluctuations. The origin of bias instability is the electronics and other components susceptible to random flickering [30]. Bias instability (B) can be determined using Equations (4.6) and (4.7).

$$\sigma^2(\tau) = \frac{2ln2}{\pi}B^2 \tag{4.6}$$

$$B = 1.505\sigma(\tau) \tag{4.7}$$

In Figure 4.10, a curve with a slope of -1/2 is fitted to ARW region and ARW is calculated as 0.028 $^\circ/\sqrt{hr}$. Another curve with a slope of 0 is fitted to the bias instability region. The corresponding Allan deviation of the fitting curve is 0.088 $^\circ/hr$ and using the formula given in Equation (4.7), bias instability is found as 0.13 $^\circ/hr$.

Chapter 5

Optimization of Digital Detection Scheme of Fiber Optic Gyroscope

5.1 Noise Analysis of Fiber Optic Gyroscope

The shot noise, electronic noise and the relative intensity noise (RIN) are the three main noise sources that determine the noise performance, i.e., ARW of a FOG. Shot noise and RIN are proportional to $\sqrt{P}$ and P, respectively, where P is the optical power at the detector. The electronic noise is not a function of P. A detailed noise analysis of fiber optic gyroscope was performed in [31]. In this section, we will investigate signal to noise ratio (SNR) for different noise types.

In a fiber optic gyroscope, if we intend to model the noise on intensity, the demodulation signals of the FOG modulated with a square-wave bias modulation ($\Delta\phi_m$) turn into the Equation (5.1) where σ_i is the noise on intensity. We also assume the responsivity of the photodetector as 1 for simplicity of equations. However, this assumption would not effect the derivations negatively.

$$I_{odd}\left(\sigma_{i,1}\right) = \frac{I_0}{2}[1 + \cos(\Delta\phi_R + \Delta\phi_m)] + \sigma_{i,1} \tag{5.1a}$$

$$I_{even}\left(\sigma_{i,2}\right) = \frac{I_0}{2}[1 + \cos(\Delta\phi_R - \Delta\phi_m)] + \sigma_{i,2} \tag{5.1b}$$

As we have also performed in Section 3.3, we first find the difference between I_{even} and I_{odd} to reach the phase due to rotation ($\Delta\phi_R$).

$$\Delta I\left(\sigma_{i,1}, \sigma_{i,2}\right) = I_{even}\left(\sigma_{i,2}\right) - I_{odd}\left(\sigma_{i,1}\right) \tag{5.2}$$

$$\Delta I\left(\sigma_{i,1}, \sigma_{i,2}\right) = \frac{I_0}{2}[\cos(\Delta\phi_R - \Delta\phi_m) - \cos(\Delta\phi_R + \Delta\phi_m)] + \sigma_{i,2} - \sigma_{i,1} \tag{5.3}$$

$$\Delta I\left(\sigma_{i,1}, \sigma_{i,2}\right) = I_0 \sin(\Delta\phi_R)\sin(\Delta\phi_m) + \sigma_{i,2} - \sigma_{i,1} \tag{5.4}$$

Since $\sigma_{i,2}$ and $\sigma_{i,1}$ are uncorrelated random variables, by using the law $\sigma^2_{X\pm Y} = \sigma^2_X + \sigma^2_Y$, we obtain Equation (5.5).

$$\Delta I\left(\sigma_i\right) = I_0 \sin(\Delta\phi_R)\sin(\Delta\phi_m) + \sqrt{2}\sigma_i \tag{5.5}$$

By small angle approximation of $\Delta\phi_R$, the equation becomes:

$$\Delta I\left(\sigma_i\right) \approx I_0 \Delta\phi_R \sin(\Delta\phi_m) + \sqrt{2}\sigma_i \tag{5.6}$$

$$\frac{\Delta I\left(\sigma_i\right)}{I_0 \sin(\Delta\phi_m)} \approx \Delta\phi_R + \frac{\sqrt{2}\sigma_i}{I_0 \sin(\Delta\phi_m)} \tag{5.7}$$

Noise on rotation rate is the second term of Equation (5.7):

$$\sigma_{\Delta\phi_R,i} \approx \frac{\sqrt{2}\sigma_i}{I_0 \sin(\Delta\phi_m)} \tag{5.8}$$

The noise can be written in terms of noise spectral density (N_{0_i}) that is the noise power per unit bandwidth:

$$\frac{\sigma_{\Delta\phi_R,i}}{\sqrt{\Delta f}} \approx \frac{\sqrt{2}N_{0_i}}{I_0 \sin(\Delta\phi_m)} \tag{5.9}$$

where Δf is electronic bandwidth. Δf can be defined as $1/2t_s$ where t_s is sample time.

As it can be seen from the Equation (5.9), the noise on intensity is a function of phase due to modulation, i.e., modulation depth.

When the modulation depth is $\pi/2$, the equation turns into:

$$\Delta\phi_m = \frac{\pi}{2} \Rightarrow \frac{\sigma_{\Delta\phi_R,i}}{\sqrt{\Delta f}} \approx \frac{\sqrt{2}N_{0_i}}{I_0} \tag{5.10}$$

As a reminder, it was also shown $I_0 = \sum I$ for $\Delta\phi_m = \pi/2$ in Section 3.3.

5.1.1 Shot Noise

Shot noise is the fundamental noise limit in the FOG. The source of shot noise is the random distribution of photons incident on the photodetector, which leads to random fluctuations in the detector output current [12]. The sound of raindrops falling onto a tin roof is a popular analogy for shot noise. The raindrops represent photons such that light/heavy rain relates to a low/high flux of photons. The formula for shot noise is:

$$\sigma_{i,shot} = \sqrt{2eI\Delta f} \tag{5.11}$$

where e is the electron charge.

Noise spectral density can be found as:

$$N_{0_{i,shot}} = \frac{\sigma_{i,shot}}{\sqrt{\Delta f}} \Rightarrow N_{0_{i,shot}} = \sqrt{2eI} \tag{5.12}$$

Using interference equation with phase due to modulation ($\Delta\phi_m$) by small angle approximation, power spectral density of shot noise becomes:

$$N_{0_{i,shot}} \approx \sqrt{eI_0[1+\cos(\Delta\phi_m)]} \tag{5.13}$$

The contribution of shot noise to the total noise on rotation rate per $\sqrt{Hz}$ can be found as follows:

$$\frac{\sigma_{\Delta\phi_R,shot}}{\sqrt{\Delta f}} \approx \frac{\sqrt{2}N_{0_{i,shot}}}{I_0\sin(\Delta\phi_m)} \tag{5.14}$$

$$\frac{\sigma_{\Delta\phi_R,shot}}{\sqrt{\Delta f}} \approx \sqrt{\frac{2e}{I_0}}\frac{\sqrt{1+\cos(\Delta\phi_m)}}{\sin(\Delta\phi_m)} \tag{5.15}$$

$$\frac{\sigma_{\Delta\phi_R,shot}}{\sqrt{\Delta f}} \approx \sqrt{\frac{e}{I_0}}\frac{1}{\sin(\Delta\phi_m/2)} \tag{5.16}$$

For $\pi/2$ modulation depth, it is written as:

$$\Delta\phi_m = \frac{\pi}{2} \Rightarrow \frac{\sigma_{\Delta\phi_R,shot}}{\sqrt{\Delta f}} \approx \sqrt{\frac{2e}{I_0}} \tag{5.17}$$

Figure 5.1 shows the normalized amplitude of intensity (or optical power), signal, sensitivity, shot noise and noise to signal ratio with respect to modulation depth. As can be seen in the figure, sensitivity and signal is a sine function of modulation depth, whereas power is the cosine function of that as we have investigated in Chapter 3.

Although shot noise is proportional to $\sqrt{P}$, noise to signal ratio is proportional to $1/\sqrt{P}$. Consequently, noise to signal ratio is decreases as the modulation depth increases. When the depth is π, i.e., power is zero, there should be no component of the shot noise on signal. However, it is not effective to work with zero signal.

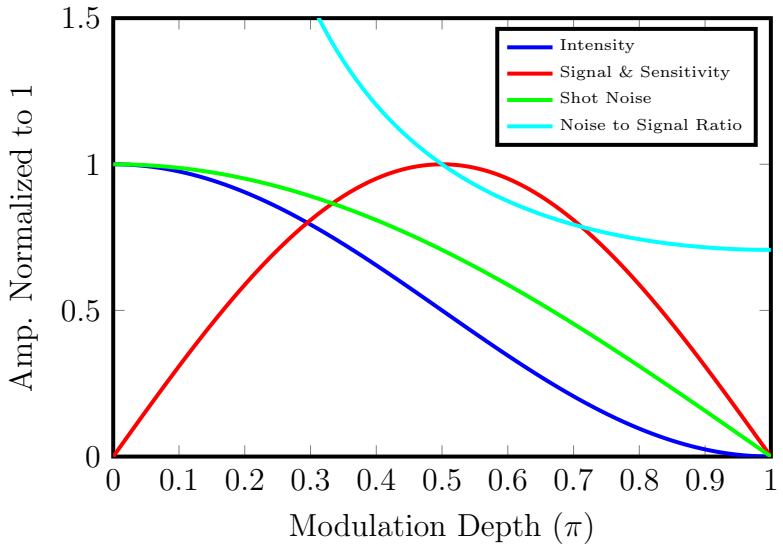

Figure 5.1: Shot noise vs. modulation depth. Noise to signal ratio is normalized to the corresponding value at $\pi/2$ modulation depth.

5.1.2 Relative Intensity Noise

In the low-coherence (broad linewidth) source the spontaneous emission gives rise to many wavelengths beating against one another, causing relative intensity noise (RIN) [32]. RIN can be calculated as given in [33].

$$\sigma_{i,RIN} = \sqrt{\frac{\Delta f}{\Delta v}} I \tag{5.18}$$

Δv is the optical linewidth that is the spectral linewidth in the frequency domain and can be obtained as:

$$\Delta v = \frac{\left[\int P(v)dv\right]^2}{\int P^2(v)dv} \tag{5.19}$$

where $P(v)$ is the power spectral density of the optical field.

It can be easily calculated with the spectral specifications of the light source via the formula given in Equation (5.20) [34].

$$\Delta v \approx \frac{c\Delta\lambda}{\lambda^2} \approx 1.4\ THz \tag{5.20}$$

Noise spectral density is:

$$N_{0_{i,RIN}} = \frac{\sigma_{i,RIN}}{\sqrt{\Delta f}} \Rightarrow N_{0_{i,RIN}} = \sqrt{\frac{1}{\Delta v}} I \tag{5.21}$$

Using the interference equation with phase due to modulation ($\Delta\phi_m$) by small angle approximation, power spectral density of RIN becomes:

$$N_{0_{i,RIN}} \approx \sqrt{\frac{1}{\Delta v}} \frac{I_0}{2}[1 + \cos(\Delta\phi_m)] \tag{5.22}$$

The contribution of RIN to the total noise on rotation rate per $\sqrt{Hz}$:

$$\frac{\sigma_{\Delta\phi_R,RIN}}{\sqrt{\Delta f}} \approx \frac{\sqrt{2} N_{0_{i,RIN}}}{I_0 \sin(\Delta\phi_m)} \tag{5.23}$$

$$\frac{\sigma_{\Delta\phi_R,RIN}}{\sqrt{\Delta f}} \approx \frac{1}{\sqrt{2\Delta v}} \frac{1 + \cos(\Delta\phi_m)}{\sin(\Delta\phi_m)} \tag{5.24}$$

$$\frac{\sigma_{\Delta\phi_R,RIN}}{\sqrt{\Delta f}} \approx \frac{1}{\sqrt{2\Delta v}} \frac{1}{\tan(\Delta\phi_m/2)} \tag{5.25}$$

For $\pi/2$ modulation depth,

$$\Delta\phi_m = \frac{\pi}{2} \Rightarrow \frac{\sigma_{\Delta\phi_R,RIN}}{\sqrt{\Delta f}} \approx \frac{1}{\sqrt{2\Delta v}} \tag{5.26}$$

Figure 5.2 shows the normalized amplitude of intensity, RIN, signal, sensitivity and noise to signal ratio as a function of modulation depth. Intensity and RIN curves are superimposed because of the fact that RIN is proportional to P. However, noise to signal is independent of intensity. When the modulation depth is zero, it reaches zero as the case in shot noise.

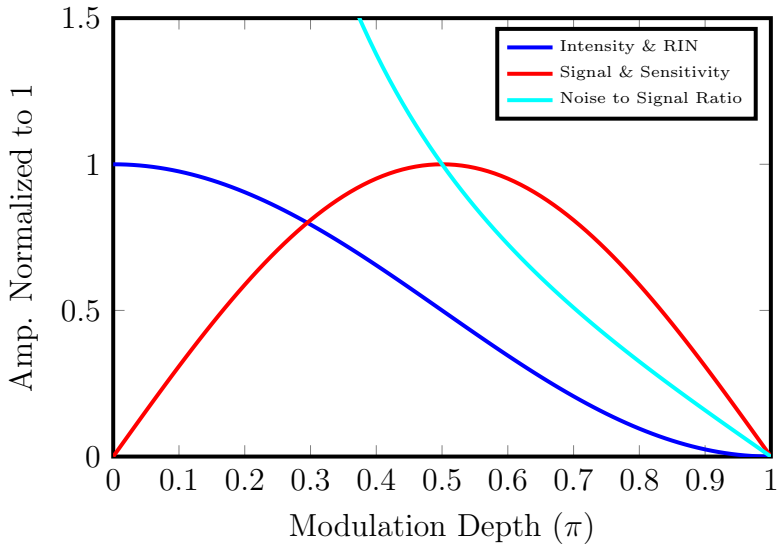

Figure 5.2: Relative intensity noise vs. modulation depth. Noise to signal ratio is normalized to the corresponding value at $\pi/2$ modulation depth.

5.1.3 Electronic Noise

The noise contributions of electronic components would be described in this section. The electronic components of the detection scheme are a photodetector, a TIA, an A/D convertor and MIOC driver consisting of a D/A convertor and a voltage amplifier.

5.1.3.1 Noise Contributions of the Photodetector and TIA

Scott et al. presented a nice model of electronic noise for a system uses both a photodiode and TIA in [35]. The equivalent circuit of a TIA driven by a photodiode is given in Figure 5.3.

The noise contributions of the photodetector and TIA can be calculated by adding uncorrelated noise sources on a mean-squared basis. The output mean-squared noise voltage spectral density of the equivalent circuit is given in Equation (5.27).

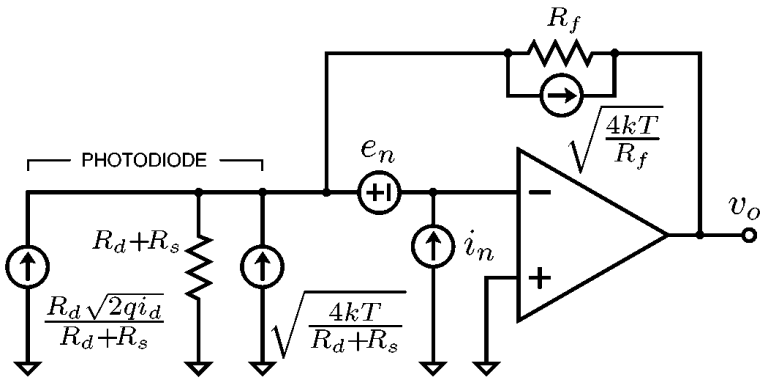

Figure 5.3: Equivalent circuit of a TIA driven by a photodiode including noise sources [35].

$$v_0^2 = \left[\underbrace{\frac{2ei_dR_d^2}{(R_s+R_d)^2}}_{\substack{\text{Dark Current}\\ \text{Shot N.}}} + \underbrace{\frac{4k_BT}{R_s+R_d}}_{\substack{\text{Photodetector}\\ \text{Johnson N.}}} + \underbrace{i_{n_{TIA}}^2}_{\substack{\text{Op-amp}\\ \text{Curr. N.}}} + \underbrace{\frac{4k_BT}{R_f}}_{\substack{\text{Feedback R.}\\ \text{Johnson N.}}} \right] R_f^2 + \underbrace{v_{n_{TIA}}^2 \left(1+\frac{R_f}{R_s+R_d}\right)^2}_{\substack{\text{Op-amp}\\ \text{Voltage N.}}} \tag{5.27}$$

where

i_d dark current,

$i_{n_{TIA}}$ op-amp input noise current spectral density,

$v_{n_{TIA}}$ op-amp input noise voltage spectral density,

k_B Boltzmann constant,

T temperature in Kelvins,

R_s photodiode series resistance,

R_d photodiode dynamic resistance,

R_f feedback resistance.

Johnson noise, also known as thermal noise, is generated by the thermal agitation of the electrons.

Table 5.1: Noise parameters of TIA

Parameters/Gain	10^2	10^3	10^4	10^5
Max. Input Current ($\pm$)	10 mA	1 mA	0.1 mA	10 μA
Upper Cut-Off Freq (-3 dB) (MHz)	200	80	14	3.5
Equ. In. Noise Volt.,$v_{n_{TIA}}$ ($^{nV}/\sqrt{Hz}$)	2.8			
Equ. In. Noise Curr.,$i_{n_{TIA}}$ ($^{pA}/\sqrt{Hz}$)	200	16	2.1	0.5
measured at	1 MHz	1 MHz	1 MHz	10 kHz

R_s is the resistance of the semiconductor material and it can generally be ignored. R_d is commonly known as shunt resistance. An ideal photodiode has an infinite shunt resistance. InGaAs detector has a shunt resistance on the order of 10 $M\Omega$. For the photodetector used in system, it is given as 1000 $M\Omega$. Some assumptions can be done by using $R_s \ll R_d$ and $R_f \ll R_d$. Photodetector Johnson noise term can be ignored since feedback resistor Johnson noise dominates it.

TIA noise has two components which are equivalent input noise current and voltage. As described in Section 4.1.2, used TIA is variable-gain. For different gain values, equivalent input noise current values are also different as seen in Table 5.1.

Noise-equivalent power of the photodetector can also be ignored since the value is extremely lower (order of 10^{-15} $^{W}/\sqrt{Hz}$) than other noise types in equivalent circuit.

After the above assumptions, Equation (5.27) becomes:

$$v_0^2 \approx \left[\underbrace{2ei_d}_{\substack{\text{Dark Current}\\ \text{Shot N.}}} + \underbrace{i_{n_{TIA}}^2}_{\substack{\text{Op-amp}\\ \text{Current N.}}} + \underbrace{\frac{4k_BT}{R_f}}_{\substack{\text{Feedback R.}\\ \text{Johnson N.}}} \right] R_f^2 + \underbrace{v_{n_{TIA}}^2}_{\substack{\text{Op-amp}\\ \text{Voltage N.}}} \tag{5.28}$$

As the gain of TIA equals to feedback thermistor, mean-squared noise current spectral density can be calculated as:

$$i_0^2 = \frac{v_0^2}{R_f^2} \approx 2ei_d + i_{n_{TIA}}^2 + \frac{4k_BT}{R_f} + \frac{v_{n_{TIA}}^2}{R_f^2} \tag{5.29}$$

The power spectral density of total noise on photodetector and TIA is:

$$N_{0_{i,PD+TIA}} \approx \sqrt{2ei_d + i_{n_{TIA}}^2 + \frac{4k_BT}{R_f} + \frac{v_{n_{TIA}}^2}{R_f^2}} \tag{5.30}$$

5.1.3.2 Noise Contribution of the A/D Converter

Average noise density, $v_{n_{ADC}}$ is given in ${}^{nv}/\sqrt{Hz}$ in the datasheet of the transceiver. The power spectral density of the noise of A/D converter is easily determined by:

$$N_{0_{i,ADC}} = \frac{v_{n_{ADC}}}{R_f} \tag{5.31}$$

5.1.3.3 Total Electronic Noise on Intensity Signal

Total power spectral density of electronic noise on intensity can be found by adding noise sources of photodetector, TIA and A/D.

$$N_{0_{i,electronic}} = \sqrt{N_{0_{i,PD+TIA}}^2 + N_{0_{i,ADC}}^2} \tag{5.32}$$

$$N_{0_{i,electronic}} = \sqrt{2ei_d + i_{n_{TIA}}^2 + \frac{4k_BT}{R_f} + \frac{v_{n_{TIA}}^2}{R_f^2} + \frac{v_{n_{ADC}}^2}{R_f^2}} \tag{5.33}$$

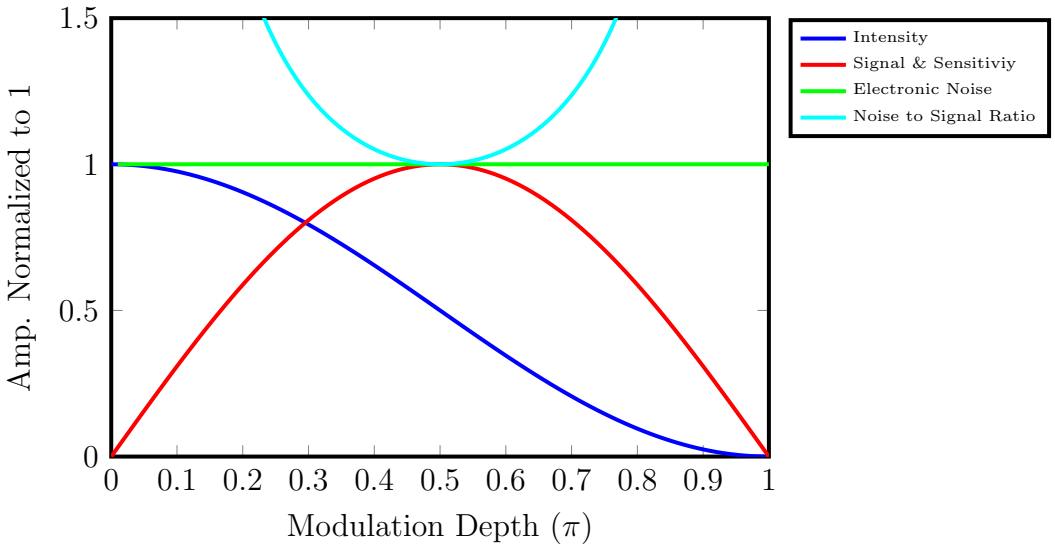

Figure 5.4: Electronic noise vs. modulation depth. Noise to signal ratio is normalized to the corresponding value at $\pi/2$ modulation depth.

The contribution of electronic noise on intensity signal to the total noise on rotation rate per $\sqrt{Hz}$ is:

$$\frac{\sigma_{\Delta\phi_R,electronic}}{\sqrt{\Delta f}} \approx \frac{\sqrt{2}N_{0_{i,electronic}}}{I_0 \sin(\Delta\phi_m)} \tag{5.34}$$

$$\frac{\sigma_{\Delta\phi_R,electronic}}{\sqrt{\Delta f}} \approx \frac{\sqrt{4ei_d + 2i^2_{n_{TIA}} + \frac{8k_BT}{R_f} + \frac{2v^2_{n_{TIA}}}{R^2_f} + \frac{2v^2_{n_{ADC}}}{R^2_f}}}{I_0 \sin(\Delta\phi_m)} \tag{5.35}$$

When the modulation depth is $\pi/2$,

$$\Delta\phi_m = \frac{\pi}{2} \Rightarrow \frac{\sigma_{\Delta\phi_R,electronic}}{\sqrt{\Delta f}} \approx \frac{\sqrt{4ei_d + 2i^2_{n_{TIA}} + \frac{8k_BT}{R_f} + \frac{2v^2_{n_{TIA}}}{R^2_f} + \frac{2v^2_{n_{ADC}}}{R^2_f}}}{I_0} \tag{5.36}$$

Figure 5.4 shows the normalized amplitude of intensity, signal, sensitivity, electronic noise and noise to signal ratio as a function of modulation depth. As can be seen also from the figure, electronic noise is independent of the intensity at the photodetector. However, it is apparent that noise to signal ratio is a function

of power and it is inversely proportional to the power. Signal reaches its lowest level when the modulation depth is $\pi/2$. Electronic noise starts to increase when modulation depth is getting away from $\pi/2$.

5.1.3.4 Noise Contribution of MIOC Driver

MIOC driving electronics consists of a D/A converter unit and a voltage amplifier that follows the D/A converter. The noise on MIOC driver would effect the phase shift due to rotation directly. Demodulated signals can be rewritten by adding the MIOC driving electronics as:

$$I_{odd}\left(\sigma_1\right) = \frac{I_0}{2}[1 + \cos(\Delta\phi_R + \Delta\phi_m + \sigma_1)] \tag{5.37a}$$

$$I_{even}\left(\sigma_2\right) = \frac{I_0}{2}[1 + \cos(\Delta\phi_R - \Delta\phi_m + \sigma_2)] \tag{5.37b}$$

The difference between I_{even} and I_{odd}:

$$\Delta I\left(\sigma_1, \sigma_2\right) = I_{even}\left(\sigma_2\right) - I_{odd}\left(\sigma_1\right) \tag{5.38}$$

$$\Delta I\left(\sigma_1, \sigma_2\right) = \frac{I_0}{2}[\cos(\Delta\phi_R - \Delta\phi_m + \sigma_2) - \cos(\Delta\phi_R + \Delta\phi_m + \sigma_1)] \tag{5.39}$$

$$\Delta I\left(\sigma_1, \sigma_2\right) = I_0 \sin\left(\Delta\phi_R + \frac{\sigma_1 + \sigma_2}{2}\right) \sin\left(\Delta\phi_m + \frac{\sigma_1 - \sigma_2}{2}\right) \tag{5.40}$$

Since $\sigma_{i,2}$ and $\sigma_{i,1}$ are uncorrelated random variables, by using the law $\sigma^2_{X\pm Y} = \sigma^2_X + \sigma^2_Y$,

$$\Delta I\left(\sigma\right) = I_0 \sin\left(\Delta\phi_R + \frac{\sqrt{2}\sigma}{2}\right) \sin\left(\Delta\phi_m + \frac{\sqrt{2}\sigma}{2}\right) \tag{5.41}$$

By small angle approximation and ignoring noise on modulation depth,

$$\Delta I\left(\sigma\right) \approx I_0 \left(\Delta\phi_R + \frac{\sqrt{2}\sigma}{2}\right) \sin\left(\Delta\phi_m\right) \tag{5.42}$$

$$\frac{\Delta I\left(\sigma\right)}{I_0 \sin\left(\Delta\phi_m\right)} \approx \Delta\phi_R + \frac{\sqrt{2}\sigma}{2} \tag{5.43}$$

Noise on rotation rate is the second term of Equation (5.43).

$$\sigma_{\Delta\phi_R,m} \approx \frac{\sqrt{2}\sigma}{2} \tag{5.44}$$

By using the fact that applying voltage with an amplitude of V_π results a phase difference of π, we obtain the following result for the noise on rotation rate per $\sqrt{Hz}$.

$$\frac{\sigma_{\Delta\phi_R,m}}{\sqrt{\Delta f}} \approx \frac{\sqrt{2}\pi N_{0_m}}{2V_\pi} \tag{5.45}$$

where N_{0_m} is the power spectral density of noise on MIOC driver.

N_{0_m} is the total noise equivalent voltage of D/A converter and voltage amplifier.

$$N_{0_m} = \sqrt{v_{n_{DAC}}^2 + v_{n_{VA}}^2} \tag{5.46}$$

Finally, the noise of MIOC driver on rotation rate per $\sqrt{Hz}$ is:

$$\frac{\sigma_{\Delta\phi_R,m}}{\sqrt{\Delta f}} \approx \frac{\pi\sqrt{2v_{n_{DAC}}^2 + 2v_{n_{VA}}^2}}{2V_\pi} \tag{5.47}$$

It is apparent from the above equations that both noise and signal to noise ratio is not dependent on intensity.

5.1.4 Total Noise

Total noise can be found by adding shot, RIN and electronic noise of the system. We need to take both electronic noise on intensity and on MIOC driver into consideration.

Noise spectral density of the system is:

$$N_0 = \sqrt{N_{0_{i,shot}}^2 + N_{0_{i,RIN}}^2 + N_{0_{electronic}}^2} \tag{5.48}$$

where $N_{0_{electronic}}$ is the total electronic noise.

The total noise on rotation rate per $\sqrt{Hz}$ is:

$$\frac{\sigma_{\Delta\phi_R}}{\sqrt{\Delta f}} = \sqrt{\left(\frac{\sigma_{\Delta\phi_R,i}}{\sqrt{\Delta f}}\right)^2 + \left(\frac{\sigma_{\Delta\phi_R,m}}{\sqrt{\Delta f}}\right)^2} \tag{5.49}$$

$$\frac{\sigma_{\Delta\phi_R}}{\sqrt{\Delta f}} = \sqrt{\left(\frac{\sigma_{\Delta\phi_R,shot}}{\sqrt{\Delta f}}\right)^2 + \left(\frac{\sigma_{\Delta\phi_R,RIN}}{\sqrt{\Delta f}}\right)^2 + \left(\frac{\sigma_{\Delta\phi_R,electronic}}{\sqrt{\Delta f}}\right)^2 + \left(\frac{\sigma_{\Delta\phi_R,m}}{\sqrt{\Delta f}}\right)^2} \tag{5.50}$$

The noise on rotation rate can be calculate in ${}^{rad}/\sqrt{Hz}$ by above expressions. However, we need to also take scale factor (SF) into consideration. ARW is usually expressed in ${}^{\circ}/\sqrt{h}$ and can be found as given in Equation (5.51).

$$ARW = \frac{\sigma_{\Delta\phi_R}}{\sqrt{\Delta f}} \cdot \frac{1}{SF} \cdot \sqrt{\frac{t_s}{\tau_{ave}}} \cdot \frac{180}{\pi} \cdot 60 \tag{5.51}$$

where τ_{ave} is the averaging or integration time in a period.

5.2 Noise Reduction Methods in Fiber Optic Gyroscope

5.2.1 Digital Integration of Signal in a Semi-period

As discussed in Chapter 4, the A/D convertor allows us to take more than one sample in a semi-period, i.e., the transit time τ.

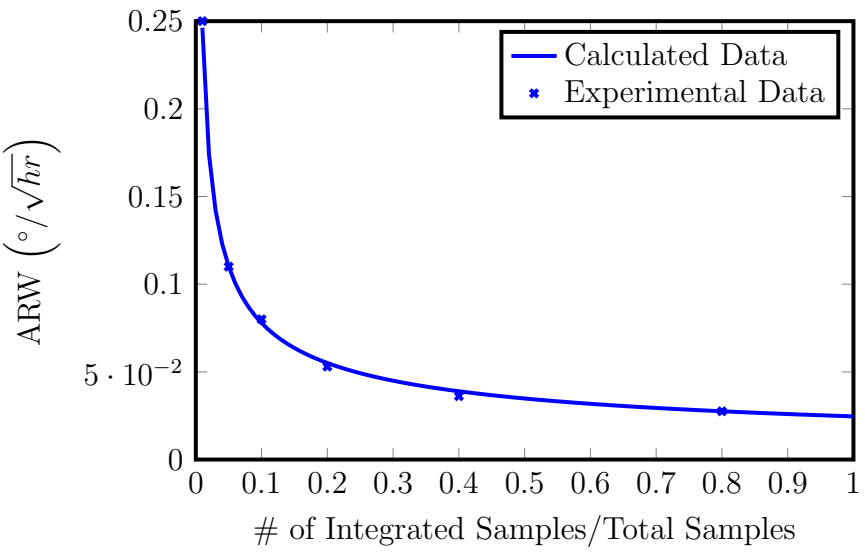

Figure 5.5: ARW vs. the ratio of number of integrated samples to total samples.

As the sample rate of the A/D convertor is 100 MS/s, we can take 100 samples in 1 μs. Since ARW is inversely proportional to the square root of averaging time, we can reduce the noise on signal by digital integration of obtained samples. However, some of the samples have high energy due to spikes (caused by square-wave bias modulation). Because of this problem, some samples are needed to be out of integration.

Another important parameter to take into consideration is hold time of the A/D converter which is actually lower then sample time of the converter.

Figure 5.5 presents both the experimental and calculated ARW value for different amount of integrated samples. We have performed experiments when the ratios of the number of integrated samples to that of total samples are 0.01, 0.05, 0.1, 0.2, 0.4 and 0.8. After 0.8, it is not very effective to take more samples because it would cause bias problems due to spikes. Experimental and calculated results are very consistent. The results meet the expectations that noise is decreasing by integration time. For the rest of calculations and experiments, 0.8 would be used as the ratio.

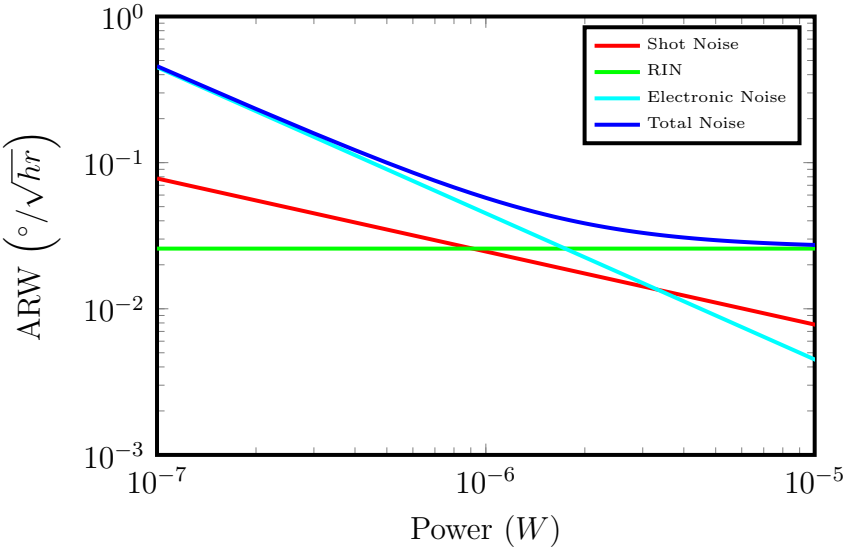

Figure 5.6: Contribution of different noise types to ARW as a function of power.

5.2.2 Required Power Analysis

The behaviors of different noise types are analyzed in Section 5.1. As a result of the analysis, while shot and electronic noise on rotation rate are dependent on power, RIN is not.

We simulate the characterization of different noise types starting from very small power value which is 0.1 μW. Shot noise and electronic noise are decreasing by power, whereas RIN is constant. Figure 5.6 presents the contributions of shot noise, RIN and electronic noise to ARW. As can be observed from the figure, RIN starts to dominate other noise types after nearly 1 μW. If RIN was smaller than that in this case, the domination of RIN would start in higher power. Consequently, the system is RIN-limited. After approximately 5 μW, power has a very limited impact on ARW.

After this analysis, we have also performed further analysis for higher power up to 1 mW. As described in Chapter 4, the used TIA is variable-gain. Therefore, it also allows to work at higher power. Figure 5.7 provides ARW values for the range of power from 1 μW to 1 mW while working at different TIA gains. ARW is decreasing as power increases for each curve. However, ARW is around

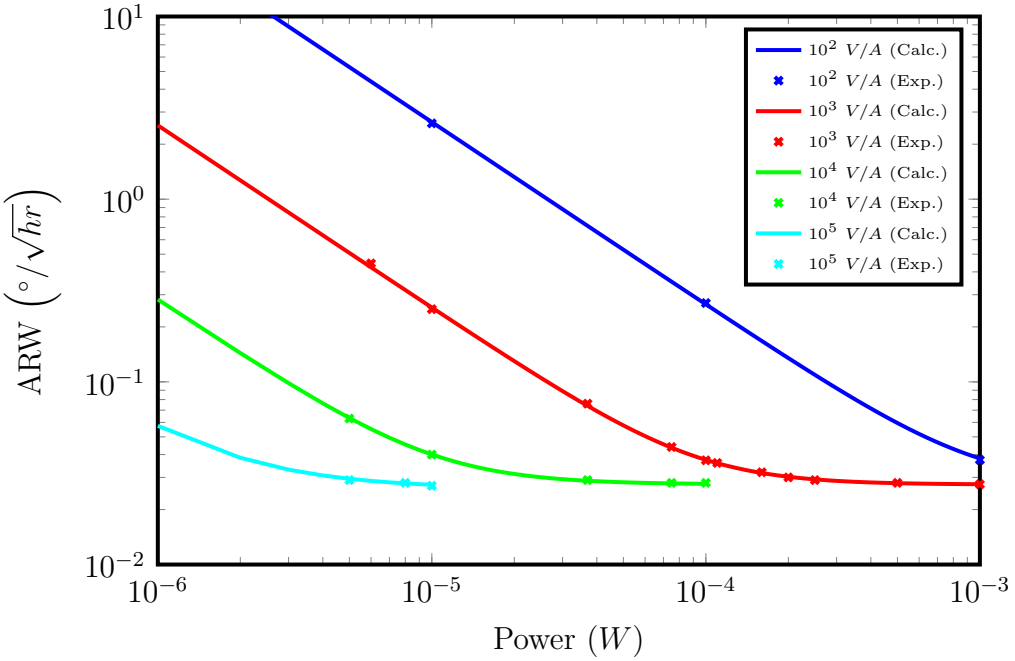

Figure 5.7: ARW vs. power at different TIA gains.

0.028 $^\circ/\sqrt{hr}$ for power from 5 μW to 1 mW if we work at proper gain. For example, working on 10 μW power with a gain of 10^5 V/A and working on 1 mW power with a gain of 10^3 V/A give similar ARW performance. We have performed several experiments and as can be seen from Figure 5.7, the experimental results fit the calculated results.

5.2.3 Optimization of Modulation Depth

As discussed above, shot noise, RIN and electronic noise depend on modulation depth. Shot noise and RIN should be theoretically zero, when the modulation depth is π which is not suitable to work. Nevertheless, electronic noise is minimum at $\pi/2$ modulation depth. As a result, the total noise should be minimized by working somewhere between $\pi/2$ and π. The idea of working with different modulation depth can be attractive as also discussed in [17] and [18].

ARW has been calculated for different modulation depths as shown in Figure 5.8. Another issue we intend to examine is the importance of power as working

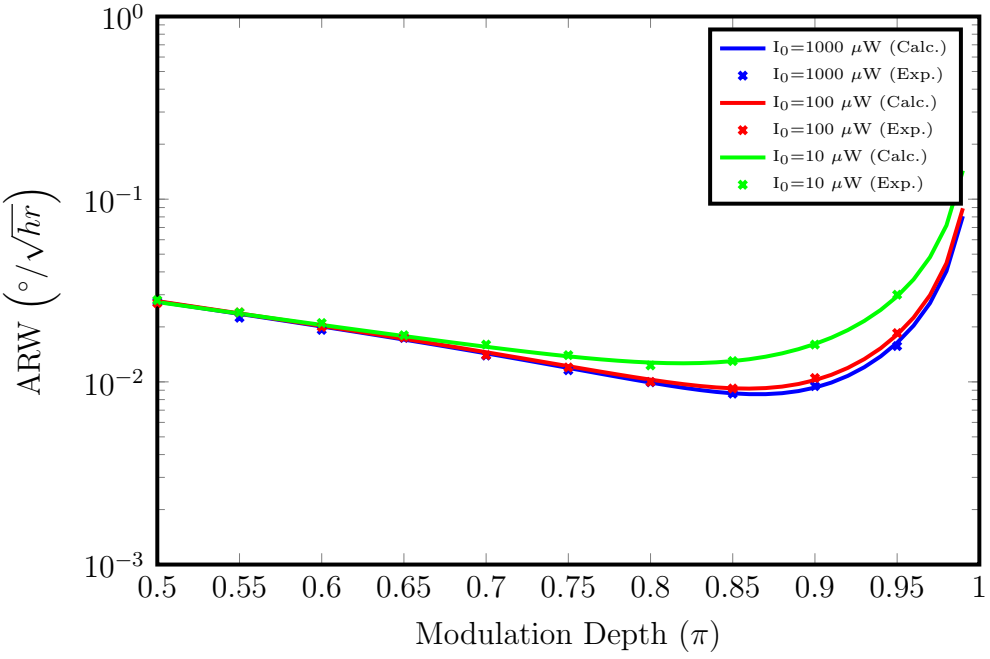

Figure 5.8: ARW vs. modulation depth for different intensities.

on different modulation depths. Therefore, we have worked with three different powers (and three different TIA gains). We have performed several experiments and obtained consistent results with calculated ones. As expected, better ARW values were achieved at somewhere between $\pi/2$ and π different.

Table 5.2 shows optimum parameters for three different powers. Optimum modulation depth is increasing as power increases. Thus, we have obtained better ARW values at higher power. However, when the power increases from 100 μW to 1 W, ARW does not changes. Apparently, 1/3 of ARW that in standard modulation scheme is obtained. The best ARW reached during this work is 0.01 $^\circ/\sqrt{hr}$ which corresponds to 0.18 $\mu rad/\sqrt{Hz}$ independent of scale factor. In conclusion, the optimization of modulation depth is a powerful method for noise reduction in a FOG.

Figure 5.9 presents Allan variance curves obtained in 1 mW output power for two different modulation depths: one is conventional $\pi/2$ modulation depth and other one is optimized modulation depth.

Table 5.2: Optimum parameters

Power (μW)	TIA Gain (V/A)	ARW ($^\circ/\sqrt{hr}$) @$\Delta\phi_m = 0.5\pi$	Opt. Mod. Depth, $\Delta\phi_{opt}$	ARW ($^\circ/\sqrt{hr}$) @$\Delta\phi_{opt}$
10	10^5	0.027	0.82π	0.013
100	10^4	0.028	0.86π	0.009
1000	10^3	0.028	0.87π	0.009

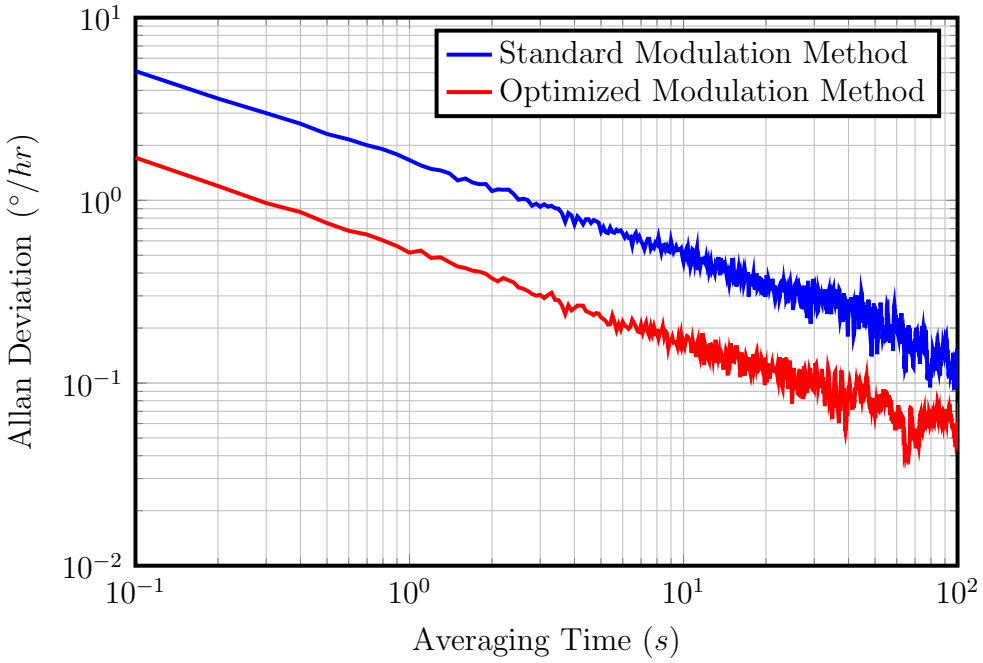

Figure 5.9: Allan variance curves obtained for standard and optimized modulation techniques.

Chapter 6

Conclusion

Fiber optic gyroscopes are intended for use in several civil and military applications. The gyroscopes are generally categorized according to their bias instability and angle random walk (ARW) performance. In this thesis, we have mainly focused on improving ARW performance of a fiber optic gyroscope.

The theory of Sagnac effect and the concept of reciprocity which are the fundamental principles of FOGs have been investigated. The optimal optical scheme of FOG has been established. Optical detection, modulation, sampling, digital signal processing and demodulation algorithms in FOG have been investigated and implemented. Some basic parameters such as scale factor, fringe visibility and π voltage of the MIOC have been measured. Moreover, ARW and bias instability of the system have been determined by Allan variance method.

Noise sources of FOG have been modeled and described in details. The effect of modulation depth and power to different noise components have been analyzed. As we have obtained a RIN-limited system, ARW has been almost same for the power from 5 μW to 1 mW.

We have reduced ARW optimizing modulation depth and reported results better than 0.01 $^\circ/\sqrt{hr}$. Considering the length and diameter of the fiber coil, it was a remarkable result. Another superiority of this thesis over the related works

in literature is that the theoretical results are supported with experimental results at each step of noise optimization. Experimental results have been perfectly following theocratical results.

The encouraging results raised the question of what could be the new improvements. Firstly, as the system has a RIN-limited performance, RIN reduction techniques can be performed to reduce total noise. In the literature, there are several works regarding RIN reduction methods [36–39]. As a future work, these methods can be investigated and implemented.

In recent FOG projects, digital closed loop scheme is widely-used. Major advantages of digital closed loop FOG are wide dynamic range and scale factor linearity. Square-wave bias modulation provides a good accuracy only around 0-point. To broaden accuracy over a wide dynamic range, closed loop technique is applied. Moreover, while ARW evaluates the short-term noise, bias instability is related to long-term stability. Closed loop scheme is expected to give better performance in terms of bias instability. In this thesis, we have implemented open loop scheme. As a future work, closed loop scheme can be implemented. However, the main problem regarding the closed loop scheme is that reset errors due to π voltage changes of the modulator should be eliminated. Second feedback loop is a very well-known method to cope this problem.

In the second feedback loop, V_π correction is performed using the reset error. For low angular rates, the time interval between two adjacent resets would be long. Therefore, V_π correction would also be done in long period. Four-state bias modulation technique has been represented in [40–42]. This new technique tracks V_π fluctuations in time, consequently improves the accuracy and scale factor linearity. For further improvement, four-state bias modulation scheme can be implemented.

Bibliography

[1] M. N. Armenise, C. Ciminelli, F. Dell'Olio, and V. M. N. Passaro, *Advances in Gyroscope Technologies*. Springer, 2010.

[2] "Full range of closed loop fiber optic gyros," Al Cielo. [Online; accessed 18-August-2013]. Available: `http://www.alcielo.com/pdf/FOGs.pdf`.

[3] M. G. Sagnac, "L'éther lumineux démontré par l'effet du vent relatif d'éther dans un interféromètre en rotation uniforme," *Comptes Rendus*, vol. 157, pp. 708–710, 1913.

[4] B. Culshaw, "The optical fibre sagnac interferometer: an overview of its principles and applications," *Measurement Science and Technology*, vol. 17, no. 1, pp. R1–R16, 2006.

[5] A. A. Michelson and H. G. Gale, "The effect of the earth's rotation rate on the velocity of light," *Astrophysical Journal*, vol. 61, pp. 140–145, 1925.

[6] A. H. Rosenthal, "Regenerative circulatory multiple-beam interferometry for the study of light-propagation effects," *J. Opt. Soc. Am.*, vol. 52, no. 10, pp. 1143–1147, 1962.

[7] W. M. Macek and D. T. M. Davis, "Rotation rate sensing with traveling-wave ring lasers," *Applied Physics Letters*, vol. 2, no. 3, pp. 67–68, 1963.

[8] J. M. López-Higuera, *Handbook of Optical Fibre Sensing Technology*. Wiley, 2000.

[9] V. Vali and R. W. Shorthill, "Fiber ring interferometer," *Appl. Opt.*, vol. 15, no. 5, pp. 1099–1100, 1976.

[10] H. Lefèvre, *The fiber-optic gyroscope*. The Artech House optoelectronics library, Artech House, 1993.

[11] "An update on KVH fiber optic gyros and their benefits relative to other gyro technologies," White paper, KVH Industries, 2012.

[12] S. Yin, P. B. Ruffin, and F. T. S. Yu, *Fiber Optic Sensors*. Optical Science and Engineering, Taylor & Francis, 2nd ed., 2008.

[13] A. D. Kersey, A. Dandridge, and W. K. Burns, "Fiber optic gyroscope technology," *Optics News*, vol. 15, no. 11, pp. 12–19, 1989.

[14] L. Zhu and X. Zhao, "New FOG detection system based on digital phase ramp feedback technique," in *Communications, Circuits and Systems and West Sino Expositions, IEEE International Conference on*, vol. 2, pp. 1770–1774, 2002.

[15] J. Han, S. Ge, and Y. Shen, "Implementation of digital detection scheme for closed-loop FOG based on DSP and FPGA," in *Instrumentation and Measurement Technology Conference, Proceedings of the IEEE*, pp. 2221–2225, 2006.

[16] M. Perlmutter, "A tactical fiber optic gyro with all-digital signal processing," in *Position Location and Navigation Symposium, IEEE*, pp. 170–175, 1994.

[17] Y. Paturel, J. Honthaas, H. Lefèvre, and F. Napolitano, "One nautical mile per month FOG-based strapdown inertial navigation system: a dream already within reach?," in *Inertial Sensors and Systems*, (Karlsruhe, Germany), pp. 12.1–12.13, 2012.

[18] G. A. Pavlath, "Method for reducing random walk in fiber optic gyroscopes," US Patent 5 530 545, 1996.

[19] S. J. Sanders, "Into the FOG: A course on fiber-optic gyroscopes." Lecture Notes, 2000.

[20] W. K. Burns, *Optical fiber rotation sensing*. Quantum Electronics - Principles and Applications Series, Academic Press, 1994.

[21] S. C. Rashleigh, R. Ulrich, W. K. Burns, and R. P. Moeller, "Polarization holding in birefringent single-mode fibers," *Opt. Lett.*, vol. 7, no. 1, pp. 40–42, 1982.

[22] D. M. Shupe, "Thermally induced nonreciprocity in the fiber-optic interferometer," *Appl. Opt.*, vol. 19, no. 5, pp. 654–655, 1980.

[23] K. Hotate and K. Tabe, "Drift of an optical fiber gyroscope caused by the Faraday effect: influence of the earth's magnetic field," *Appl. Opt.*, vol. 25, no. 7, pp. 1086–1092, 1986.

[24] K. Böhm, K. Petermann, and E. Weidel, "Sensitivity of a fiber-optic gyroscope to environmental magnetic fields," *Opt. Lett.*, vol. 7, no. 4, pp. 180–182, 1982.

[25] M. J. F. Digonnet, *Rare-Earth-Doped Fiber Lasers and Amplifiers*. Optical Engineering Series, Marcel Dekker Inc., 2nd ed., 2001.

[26] "DET01CFC user guide," Thorlabs, 2012.

[27] "NI 5781R user guide and specifications," National Instruments, 2010.

[28] "AD9777 datasheet," Analog Devices, 2006.

[29] B. E. A. Saleh and M. C. Teich, *Fundamentals of Photonics*. Wiley Series in Pure and Applied Optics, Wiley, 2nd ed., 2007.

[30] "IEEE standard specification format guide and test procedure for single-axis interferometric fiber optic gyros," IEEE Std 952-1997, 1998.

[31] B. Osunluk, "Double closed loop interferometric fiber optic gyroscope simulator design," M.Sc. thesis, Middle East Technical University, 2011.

[32] H. F. Taylor, "Intensity noise and spontaneous emission coupling in superluminescent light sources," *Quantum Electronics, IEEE Journal of*, vol. 26, no. 1, pp. 94–97, 1990.

[33] W. K. Burns, R. P. Moeller, and A. Dandridge, "Excess noise in fiber gyroscope sources," *Photonics Technology Letters, IEEE*, vol. 2, no. 8, pp. 606–608, 1990.

[34] F. J. Duarte, *Tunable Laser Optics*. Elsevier Science, 2003.

[35] R. P. Scott, C. Langrock, and B. Kolner, "High-dynamic-range laser amplitude and phase noise measurement techniques," *Selected Topics in Quantum Electronics, IEEE Journal of*, vol. 7, no. 4, pp. 641–655, 2001.

[36] K. M. Killian, M. Burmenko, and W. Hollinger, "High performance fiber optic gyroscope with noise reduction," in *SPIE Conference on Fiber Optic and Laser Sensors XII*, vol. 2292, pp. 255–263, 1994.

[37] F. Hakimi and J. D. Moores, "RIN-reduced light source for ultra-low noise interferometric fibre optic gyroscopes," *Electronics Letters*, vol. 49, no. 3, pp. 205–207, 2013.

[38] S. M. Bennett, "Apparatus and method for electronic RIN reduction in fiber-optic sensors utilizing filter with group delay," US Patent 6 763 153, 2004.

[39] L. K. Strandjord, G. W. Adams, and D. Ang, "System for suppression of relative intensity noise in a fiber optic gyroscope," US Patent 6 204 921, 2001.

[40] S. Chen, J. Cheng, and W. Gao, "A phase modulation method for improving the scale factor stability of fiber-optic gyroscope," in *Mechatronics and Automation, IEEE International Conference on*, pp. 37–42, 2008.

[41] L. Xuyou, Z. Yong, and Z. Chen, "Five points modulation in closed loop fiber optic gyroscope," in *Wireless Communications, Networking and Mobile Computing, 5th International Conference on*, pp. 1–3, 2009.

[42] F. Sun, L. Wang, and G. Wang, "Study on the drift of modulated phase in interference fiber optic gyroscope," *Journal of Computers*, vol. 5, no. 3, 2010.